The Astrophysical Journal, 824:57 (19pp), 2016 June 10 doi:10.3847/0004-637X/824/1/57

IN-N-OUT: THE GAS CYCLE FROM DWARFS TO SPIRAL GALAXIES

Charlotte R. Christensen[1], Romeel Davé[2,3,4], Fabio Governato[5], Andrew Pontzen[6], Alyson Brooks[7], Ferah Munshi[8], Thomas Quinn[5], and James Wadsley[9]
[1] Physics Department, Grinnell College, 1116 Eighth Avenue, Grinnell, IA 50112, USA; christenc@grinnell.edu
[2] University of the Western Cape, Bellville, Cape Town 7535, South Africa
[3] South African Astronomical Observatories, Observatory, Cape Town 7925, South Africa
[4] African Institute for Mathematical Sciences, Muizenberg, Cape Town 7945, South Africa
[5] Astronomy Department, University of Washington, 3910 15th Avenue NE, Seattle, WA 98195-0002, USA
[6] Department of Physics and Astronomy, University College London, Gower Street, London, WC1E 6BT, USA
[7] Department of Physics and Astronomy, Rutgers University, the State University of New Jersey, 136 Frelinghuysen Road, Piscataway, NJ 08854-8019, USA
[8] Department of Physics and Astronomy, University of Oklahoma, 440 W. Brooks Street, Norman, OK 73019, USA
[9] Department of Physics and Astronomy, McMaster University, 1280 Main Street W, Hamilton, ON L8S 4L8, Canada
Received 2015 July 9; accepted 2016 March 23; published 2016 June 13

ABSTRACT

We examine the scalings of galactic outflows with halo mass across a suite of 20 high-resolution cosmological zoom galaxy simulations covering halo masses in the range $10^{9.5}$–10^{12} $M_{\odot}$. These simulations self-consistently generate outflows from the available supernova energy in a manner that successfully reproduces key galaxy observables, including the stellar mass–halo mass, Tully–Fisher, and mass–metallicity relations. We quantify the importance of ejective feedback to setting the stellar mass relative to the efficiency of gas accretion and star formation. Ejective feedback is increasingly important as galaxy mass decreases; we find an effective mass loading factor that scales as $v_{\rm circ}^{-2.2}$, with an amplitude and shape that are invariant with redshift. These scalings are consistent with analytic models for energy-driven wind, based solely on the halo potential. Recycling is common: about half of the outflow mass across all galaxy masses is later reaccreted. The recycling timescale is typically ∼1 Gyr, virtually independent of halo mass. Recycled material is reaccreted farther out in the disk and with typically ∼2–3 times more angular momentum. These results elucidate and quantify how the baryon cycle plausibly regulates star formation and alters the angular momentum distribution of disk material across the halo mass range where most cosmic star formation occurs.

Key words: galaxies: evolution – galaxies: general – galaxies: structure – intergalactic medium – ISM: jets and outflows – methods: numerical

1. INTRODUCTION

1.1. Evidence for Outflows

Galactic outflows driven by stellar feedback have emerged over the past decade as an integral aspect of how galaxies form and evolve. Outflows are commonly detected in star-forming galaxies at $z > \sim 0.5$ (e.g., Pettini et al. 2003; Shapley et al. 2003; Weiner et al. 2009; Steidel et al. 2010; Genzel et al. 2011; Rubin et al. 2014), and preliminary estimates of the mass-loss rate indicate that it is of the same order as the star formation rate (e.g., Erb 2008; Steidel et al. 2010; Genzel et al. 2013). The ubiquity of outflows during this cosmic period and their lack of association with active galactic nuclei (e.g., Shapley et al. 2003) suggest that they are not associated with a particular phase of galaxy formation. Instead, it appears that these galactic outflows are common in galaxies lying on the star-forming galaxy main sequence and are likely driven by their high star formation rates or some related property.

Theoretical models of galaxy formation have also found it increasingly necessary to invoke stellar-feedback-driven galactic outflows. Strong and ubiquitous outflows first appeared in galaxy formation simulations in order to explain observations of widespread metal enrichment in the intergalactic medium (IGM) at early epochs (Aguirre et al. 2001; Oppenheimer et al. 2006). However, it was soon recognized that these same outflows had a considerable impact on the properties of galaxies themselves, such as their stellar and baryonic content, their metallicity, their mass distribution, and the state of the circumgalactic medium (CGM). Today, the majority of successful galaxy formation models, be they hydrodynamic or semianalytic (e.g., Somerville et al. 2015), include stellar-feedback-driven galactic outflows as a central feature.

1.2. Impact of Outflows on Galaxies

Galactic outflows have a strong impact on the growth of the stellar and gaseous content of galaxies. First, mass loss limits the amount of baryons in the disk of galaxies, thereby impacting the observed baryonic mass fraction within the halos of galaxies (e.g., Davé 2009) and the total stellar and disk gas mass of the galaxies (e.g., Scannapieco et al. 2012). Mass loss, in combination with heating of the interstellar medium (ISM) by feedback (e.g., Brooks et al. 2007), also impacts the observed galaxy stellar mass function by limiting the amount of star formation in the disk of the galaxy (Springel & Hernquist 2003b; Davé et al. 2011). By reducing the amount of gas available for star formation, outflows mitigate the overcooling problem wherein too large a fraction of baryons condenses into stars (White & Rees 1978; Balogh et al. 2001; Davé et al. 2001). Moreover, stellar-feedback-driven outflows are frequently invoked to explain the sub-L^* portion of the stellar mass–halo mass relation (e.g., Shankar et al. 2006), and the simulations most successful in reproducing the stellar mass–halo mass relation typically employ strong stellar feedback (Stinson et al. 2012; Aumer et al. 2013; Hopkins et al. 2014). The efficiency of outflows across a range of galaxy

masses is therefore key to determining the stellar and baryonic mass for different mass halos.

As well as globally impacting the baryons within galaxies, outflows play an important role in determining the distribution of matter. For example, the stellar feedback that drives outflows delays star formation, which results in less angular momentum loss during galaxy mergers and therefore less centrally concentrated galaxies (White & Rees 1978; Dekel & Silk 1986; Navarro & Steinmetz 1997; Robertson et al. 2004; Okamoto et al. 2005; Scannapieco et al. 2008; Governato et al. 2009).

In addition to being an agent for reducing angular momentum loss, stellar feedback is now also considered a mechanism for removing low angular momentum baryons in galaxies. This removal is necessary for the modeling of realistic galaxies: while the overall specific angular momentum of disks is comparable to that of their parent dark matter halos (Fall & Efstathiou 1980; Dalcanton et al. 1997; Mo et al. 1998), the observed *distribution* of the specific angular momentum in any given disk differs from predictions based on pure angular momentum conservation. In particular, observed galaxies are deficient in low angular momentum material compared to simple disk collapse models (van den Bosch et al. 2001). Strong galactic winds were first posited as a mechanism for removing low angular momentum material in Binney et al. (2001), and recent simulations have demonstrated that stellar feedback preferentially removes low angular momentum material from galaxies (Governato et al. 2010; Brook et al. 2011, 2012b; Macciò et al. 2012; Übler et al. 2014). The loss of low angular momentum baryons results in bulgeless dwarf galaxies (Governato et al. 2010) and spiral galaxies with more realistic central baryonic distributions (Brook et al. 2012a; Anglés-Alcázar et al. 2014; Christensen et al. 2014a).

While outflows are typically thought of as a way to remove material, the reaccretion of that material (wind recycling) also impacts galaxy evolution. Some outflowing material must be transferred to the diffuse IGM in order to explain observations (e.g., Cowie et al. 1995) of metal-line absorption (Oppenheimer et al. 2006, 2012; Cen & Chisari 2011). However, in many cases the outflows are thought not to escape the CGM, but to instead return to the galaxy on relatively short timescales. This so-called wind recycling adds to the pristine accretion from the IGM and to the accretion of gas already bound in galaxies (i.e., mergers). The recycling of previously ejected wind material can be a key factor in setting the galaxy stellar mass function (e.g., Oppenheimer et al. 2010; Bower et al. 2012). It is also thought that fountaining gas gains angular momentum through interactions within the halo environment before being reaccreted (Marasco et al. 2012), which further shifts the angular momentum distribution of the disk baryons to higher values (Brook et al. 2012a).

1.3. The Analysis of Outflows Presented Here

Together, inflows, outflows, and wind recycling govern many of the key physical properties of galaxies (e.g., Davé et al. 2012). Therefore, it is critical to understand the operation of the baryon cycle, including the scaling of the mass loading factor with galactic properties; the relative rates of outflowing, accreted, and recycled gas; and the source and eventual destination of outflowing material. Hydrodynamic simulations of galaxy growth are a valuable tool for this, because the inherently dynamical nature of the baryon cycle requires a fully dynamical model to capture it properly. Such simulations must be set within a fully cosmological context, since the accretion is cosmologically driven. Furthermore, the details of the complex interactions between inflows, stellar feedback, outflows, and ambient halo gas strongly motivate very high numerical resolution. These requirements are a challenge for current galaxy formation models, one that is only recently starting to be met using cosmological "zoom" simulations, in which an individual galaxy is resimulated at much higher resolution within a larger cosmological volume.

In this paper we investigate the detailed dynamics of inflow and outflow processes using a suite of cosmological zoom simulations. We take advantage of the particle-based nature of our smoothed particle hydrodynamics (SPH) simulations run with the Gasoline code to directly track all mass movement in and out of the disk and CGM. This particle tracking enables us to directly study recycling and to identify the source and future trajectory of individual parcels of gas. We analyze high-resolution simulations of 20 spiral and dwarf galaxies that span 2.5 orders of magnitudes in virial mass, all simulated with the same physics and comparable numerical resolution. Our work improves on previous particle tracking analyses that have focused either on low-resolution (non-zoom) simulations of many galaxies (Oppenheimer et al. 2010) or on a few simulations of similar-mass galaxies (Brook et al. 2012a; Übler et al. 2014; Woods et al. 2014) and complements non-particle-tracking studies of galactic winds (Muratov et al. 2015).

Our simulations self-consistently generate outflows from the available supernova (SN) energy using a methodology that has been shown to successfully reproduce a wide variety of galaxy observations. In this method, the transfer of stellar feedback energy depends only on the local properties of the ISM, and since the feedback model is ignorant of the host galaxy properties, outflow trends with mass result from the dynamics of the simulation. This analysis enables us to independently study inflows, outflows, and recycling as a function of galaxy mass, which allows a deeper investigation into the underlying physical processes that govern the baryon cycle. The details of baryon cycling presented here do depend on our methodology for driving outflows and may vary for different choices of physical models (see, e.g., Keller et al. 2015; Muratov et al. 2015). Nonetheless, our results are of particular interest since our outflow driving model yields a viable match to numerous key observational constraints, as we will show.

Our paper is organized as follows. In Section 2 we describe the simulations used and the particle-tracking analysis used to determine outflows. We justify our simulation models in Section 3.1 by comparing their global properties to observed trends. In Sections 3.2–3.4, we analyze the efficiency of various forms of feedback across galaxy mass. We examine gas recycling and the characteristics of reaccreted material in Sections 3.5–3.7. We discuss our results in light of other models and numerical concerns in Section 4.

2. SIMULATION AND ANALYSIS

We compared the properties of outflows across a set of 20 field galaxies with final virial masses between $10^{9.5}$ and 10^{12} $M_{\odot}$ that were simulated using the N-body + SPH code Gasoline (Wadsley et al. 2004). Gasoline is an SPH extension to pkdgrav (Stadel 2001), a parallel, gravity-tree-based N-body code. The simulations were integrated to a redshift of zero in a fully cosmological, ΛCDM context using WMAP3 (Spergel et al. 2007) parameters: $\Omega_0 = 0.24$, $\Lambda = 0.76$, $h = 0.73$, $\sigma_8 = 0.77$.

Table 1
Properties of the Galaxies at $z = 0$

Simulation Name	Softening Length (pc)	Gas Particle Mass ($M_\odot$)	Halo ID	Virial Mass ($M_\odot$)	Gas Mass in R_{vir} ($M_\odot$)	Cold Gas Mass ($M_\odot$)	Stellar Mass ($M_\odot$)	V_f (km s^{-1})
	(1)	(2)	(3)	(4)	(5)	(6)	(7)	(8)
h799	87	3.3×10^3	1[a,b,c]	2.4×10^{10}	1.4×10^9	2.5×10^8	1.4×10^8	55
			4	6.8×10^9	4.1×10^7	1.0×10^7	1.8×10^7	33
			6	4.4×10^9	3.9×10^7	2.6×10^7	3.5×10^6	27
h516	87	3.3×10^3	1[a,b,cd,	3.8×10^{10}	2.3×10^9	5.5×10^8	2.5×10^8	67
			2	1.5×10^{10}	3.7×10^8	4.6×10^7	8.1×10^7	34
h986	170	2.7×10^4	1[b,c]	1.9×10^{11}	1.7×10^{10}	3.5×10^9	4.5×10^9	103
			2	5.9×10^{10}	3.2×10^9	7.4×10^8	1.2×10^9	77
			3	3.8×10^{10}	2.4×10^9	5.4×10^8	4.6×10^8	76
			8	3.8×10^{10}	6.4×10^7	1.3×10^7	4.0×10^7	35
			15	4.4×10^9	8.7×10^7	2.7×10^8	6.2×10^6	29
			16	3.2×10^9	3.0×10^7	1.1×10^8	2.3×10^6	27
h603	170	2.7×10^4	1[b,c]	3.4×10^{11}	3.1×10^{10}	4.2×10^9	7.8×10^9	115
			2[b]	1.0×10^{11}	6.1×10^9	7.8×10^8	3.8×10^9	75
			3	2.9×10^{10}	1.8×10^8	1.8×10^8	3.9×10^8	50
h258	170	2.7×10^4	1[b,e]	7.7×10^{11}	5.6×10^{10}	5.7×10^9	4.5×10^{10}	182
			4	1.1×10^{10}	1.4×10^8	6.2×10^7	5.9×10^7	43
h285	170	2.7×10^4	1[b]	8.8×10^{11}	6.3×10^{10}	8.5×10^9	4.6×10^{10}	164
			4	3.4×10^{10}	1.2×10^9	1.5×10^8	3.9×10^8	64
			9	1.2×10^{10}	3.1×10^8	1.3×10^8	5.4×10^7	52
h239	170	2.7×10^4	1[b]	6.8×10^{11}	8.1×10^{10}	6.2×10^9	4.5×10^{10}	165

Notes. Column (5) lists the total mass of gas within the virial radius, while column (6) lists the mass of only H I, H_2, and He I. The stellar mass listed in column (7) is calculated directly from the simulation.
[a] Appears in Governato et al. (2012).
[b] Appears in Munshi et al. (2013).
[c] Appears in Christensen et al. (2014b).
[d] Appears in Christensen et al. (2012).
[e] Appears in Zolotov et al. (2012).

All 20 galaxies are central galaxies selected from a set of seven simulations. In order to achieve significantly higher resolution while still modeling the effects of the large-scale environment, we used the "zoom-in" volume renormalization technique (Katz & White 1993). More specifically, to create the initial conditions for these simulations, we selected seven field-like regions from two uniform dark-matter-only simulations, one representing a 25^3 Mpc^3 volume and the other a 50^3 Mpc^3 volume. These regions (0.05% of the total volume) were then resimulated at higher resolution in the context of the larger dark-matter-only simulation. The final sample galaxies had massive dark particle contamination of less than 0.07% of their total dark matter mass, and 11 of the galaxies were completely free from contamination. The force spline softening lengths are either $\epsilon = 87$ or 170 pc, and the particle masses for the dark matter, gas, and stars (at their formation) are, respectively, 1.6 (13) $\times 10^4$, 3.3 (27.0) $\times 10^3$, and 1.0 (8.0) $\times 10^3 M_\odot$. The simulations have a minimum smoothing length of 0.1ϵ, which is sufficient to resolve the disks of galaxies and the giant molecular clouds within which stars form. All the simulations used a force accuracy criterion of $\theta = 0.725$ and a Courant condition of $\eta_C = 0.4$. Particle time steps were required to satisfy $\Delta t = \eta\sqrt{\eta_i/a_t}$, where η_i is the particle's gravitational softening, a_i is the particle's acceleration, and $\eta = 0.195$. The parameters used to simulate the galaxies and their final properties at $z = 0$ are listed in Table 1.

We integrate over the H and He chemical networks to produce non-equilibrium ion abundances and H_2 abundance (Christensen et al. 2012). H_2 forms both on dust grains, assuming a fixed dust-to-metallicity ratio and a clumping factor of 10 (Wolfire et al. 2008; Gnedin et al. 2009), and via H^-, following the minimal model of Abel et al. (1997). Photoionization and heating rates of H and He are calculated assuming a set redshift-dependent cosmic ultraviolet (UV) background (Haardt & Madau 2005).[10] The Lyman–Werner radiation, which is responsible for H_2 photo-dissociation, is calculated based on emission from nearby stellar particles (Christensen et al. 2012). H_2 is shielded from dissociating radiation through both self-shielding and dust shielding (Draine & Bertoldi 1996; Glover & Mac Low 2007; Gnedin et al. 2009), using the smoothing lengths of particles for the column lengths. Similarly, H I is shielded from photoionizing radiation by dust.

Cooling channels include collisional ionization (Abel et al. 1997), H_2 collisions, radiative recombination (Black 1981; Verner & Ferland 1996), photoionization, bremsstrahlung, and H I, H_2, and He line cooling (Cen 1992). Additional cooling takes place via metal lines (Shen et al. 2010). The metal-line cooling rates used in the code are tabulated based on the gas temperature, density, and metallicity and the cosmic UV background. These rates are computed using CLOUDY (version 07.02; Ferland et al. 1998) under the assumptions that the gas was in ionization equilibrium and optically thin to UV radiation.

GASOLINE separately follows both the oxygen and iron abundances of gas particles and the total metal production. These metals are injected into the gas by Type I and II SNe following

[10] Haardt & Madau (2005) refers to an unpublished updated version of Haardt & Madau (1996), specified in CLOUDY (Ferland et al. 1998) as "table HM05."

Raiteri et al. (1996) and distributed across the smoothing sphere. They are also injected by stellar winds using a model for mass loss that follows Weidemann (1987) and assumes that the metallicity is that of the stellar particle. Metals are further distributed throughout the gas by diffusion (Shen et al. 2010).

Star formation proceeds probabilistically, according to the gas density and H_2 fraction. The dependency on H_2 represents the observed connection between the star formation rate and the local H_2 abundance (e.g., Bigiel et al. 2008). The probability p of a given gas particle forming a star is

$$p = \frac{m_{\rm gas}}{m_{\rm star}}\left(1 - e^{-c^*\frac{X_{\rm H_2}}{X_{\rm H_2}+X_{\rm H\,I}}\Delta t/t_{\rm dyn}}\right), \quad (1)$$

where $m_{\rm gas}$ is the mass of the gas particle, $m_{\rm star}$ is the mass of the potential star, $c^* = 0.1$ is the star-forming efficiency, $X_{\rm H_2}$ and $X_{\rm H\,I}$ are the mass fractions of the particle in the form of H_2 and H I, respectively, Δt is the time step, and $t_{\rm dyn}$ is the dynamical time. Star formation is allowed to proceed only in gas particles that are denser than 0.1 amu cm^{-3} and colder than 10^3 K. However, the dependency on the H_2 abundance made these two constraints largely irrelevant since almost all stars form at gas densities greater than 10 amu cm^{-3}.

SN feedback is incorporated using the "blastwave" approach (Stinson et al. 2006), in which the theoretical solution to a blast-wave explosion in a medium of a given density and pressure is used to determine the spatial extent of the feedback. In this approach, energy is distributed to nearby gas particles that lie within the maximum radius of the SN blastwave (Chevalier 1974). The cooling of these affected particles is disabled for a period of time equal to the theoretical lifetime of the hot, low-density shell produced during the momentum-conserving phase of the SN remnant (McKee & Ostriker 1977). Typically, these periods of time are on the order of several times 10^7 yr. The total amount of energy deposited in the ISM is the canonical 10^{51} erg per SN.

The blastwave recipe differs from many other subgrid feedback recipes (e.g., Springel & Hernquist 2003a; Davé et al. 2011; Scannapieco et al. 2012) in that wind particles are not provided with an artificial kick. Even when cooling is disabled for the feedback-affected gas particles, they continue in all other ways to interact hydrodynamically with the rest of the simulation. Additionally, the feedback depends only on the local gas properties; it is independent of the large-scale properties of the galactic halo. This feedback recipe does not include a separate model for other forms of stellar feedback, such as radiation pressure, which may help drive a galaxy wind either by adding additional momentum to the gas or causing the gas to be more responsive to SN feedback (Stinson et al. 2012; Hopkins et al. 2014). As such, this efficient transfer of SN energy into the ISM and the temporary delay of cooling are best interpreted as a model for the *total stellar* feedback from all processes related to young stars. In Section 4, we discuss the possible impacts of excluding other forms of stellar feedback.

2.1. Postprocessing Analysis

Individual halos are identified in each snapshot using AMIGA's HALO FINDER (Gill et al. 2004; Knollmann & Knebe 2009),[11] which uses a grid hierarchy to identify areas of overdensity and iteratively removes gravitationally unbound particles from the prospective halos. The virial radius, $R_{\rm vir}$, is defined to be the radius for which the average halo density is some multiple of the background density. This value for the average halo density evolves with redshift but is approximately equal to 100 times the critical density. In determining the evolution of the halo, we use a merger tree to trace the main progenitor back in time. At each snapshot, the main progenitor is defined to be the halo in the previous step that contains the majority of the particles in the current halo.

In order to verify the properties of the simulated galaxies, we make as direct a comparison to observations as possible (e.g., see Section 3.1 for the comparisons to the stellar mass–halo mass, Tully–Fisher, and mass–metallicity relationships). This comparison requires the generation of mock-photometric magnitudes, which was accomplished using the ray-tracing radiative transfer program SUNRISE (Jonsson 2006). Magnitudes in different bands were calculated for the galaxy oriented at a 45° angle with the midplane defined by the angular momentum axes of the gas within 5 kpc of the center (comoving). Face-on SUNRISE-generated images of all the galaxies in Sloan Digital Sky Survey (SDSS) *g*, *r*, and *i* filters are shown in Figure 1.

Table 1 lists the global properties of the halos, including virial, total gas, cold gas, and stellar mass for each of the halos at a redshift of zero. The stellar mass listed is the total stellar mass within the virial radius and is calculated directly from the simulation (rather than from mock-photometric observations). We list both the total gas mass (mass of gas particles within $R_{\rm vir}$) and cold gas mass in order to distinguish between the entirety of the gas mass and the fraction of it that is easily observable. Here the cold gas mass was defined to be gas mass in the form of H I, H_2, and He I.

2.1.1. Particle Tracking

In order to study the baryon cycle within galaxies in detail, the gas must be followed as it is accreted to and is ejected from the disk. As such, we determine gas accretion and gas loss through particle tracking. Essentially, we divide the gas between disk, halo, and IGM for each of the snapshots, and then the movement between these phases marks inflow and outflow. In addition to allowing us to identify gas recycling, this particle tracking enables us to determine the source of gas outflows.

We used particle tracking to identify *accreting* and *outflowing* gas and further subdivided the outflowing gas into *ejected* gas that became dynamically unbound from the disk and *expelled* gas that escaped the halo. Our method for identifying these incidents is as follows. First, at each snapshot we determine the gas particles that are in the main halo and the disk of the galaxy. Gas particles are considered part of the galaxy if the halo finder determined them to be a member of either the main halo or one of its satellites. Gas particles are considered part of the disk of the galaxy during a snapshot if they meet all of the following criteria:

1. have a density $n \geqslant 0.1$ amu cm^{-3};
2. have a temperature $T \leqslant 1.2 \times 10^4$ K;
3. are within 3 kpc of the midplane of the galaxy.

The density and temperature cuts select for the cool ISM phase of gas, while the spatial cut excludes the ISM of satellite galaxies. For this analysis, we focus on tracking particles since $z = 3$.

[11] AMIGA's HALO FINDER is available for download at http://popia.ft.uam.es/AHF/Download.html.

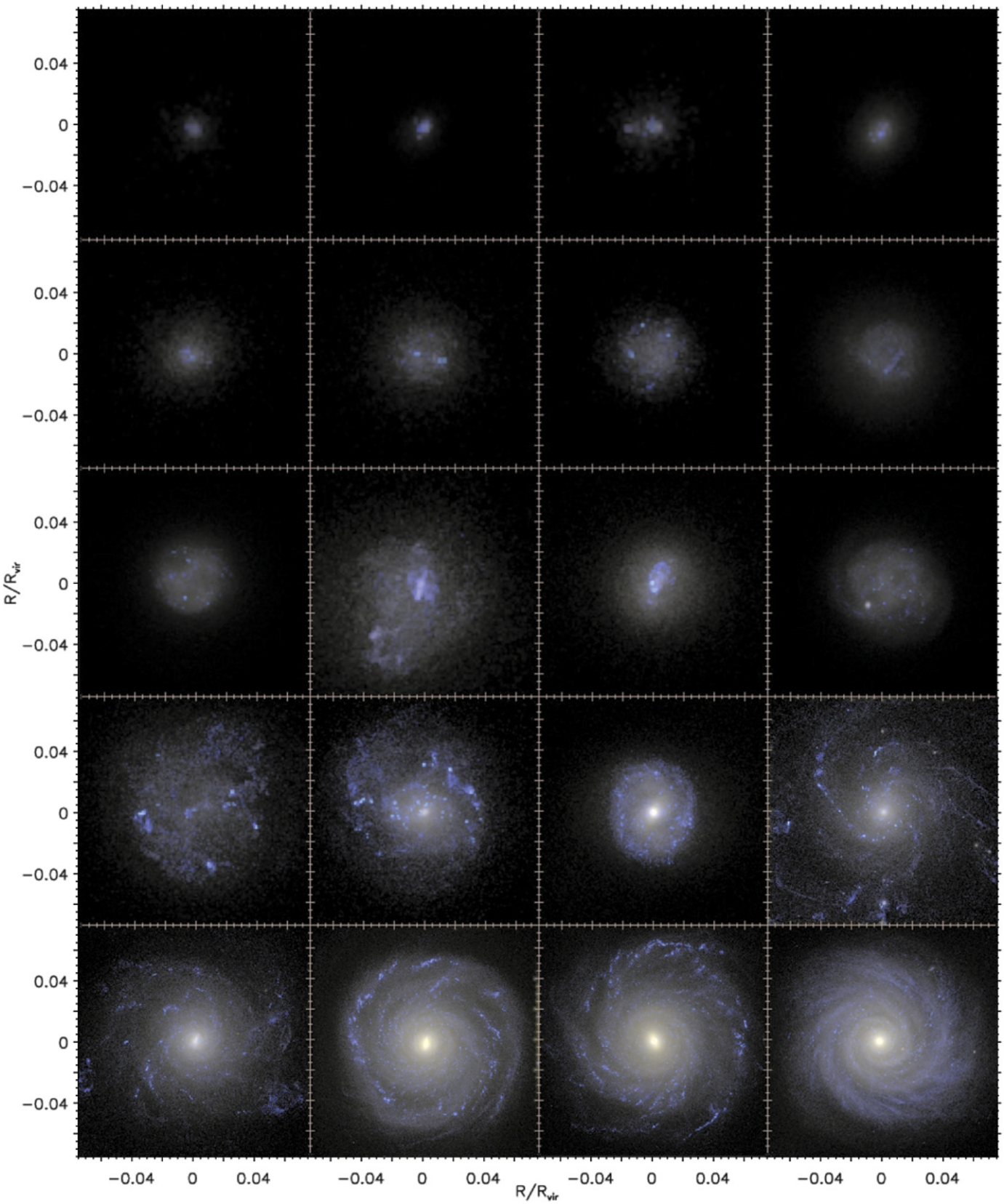

Figure 1. Simulated observations of the sample of galaxies in SDSS *r*, *g*, and *i* bands at $z = 0$ and ranked by mass. All galaxies are shown face-on, and the images were generated using SUNRISE.

Instances of gas *accretion* include both the first snapshot in which a gas particle is identified as part of the disk and each time it reenters the disk.

Ejected gas is defined as the gas particles that not only stop being identified as part of the disk but also become gravitationally unbound from the *baryonic* disk of the galaxy.

These ejected particles have, at some snapshot subsequent to leaving the disk, a kinetic energy greater than the gravitational potential from the combined disk gas plus stellar mass (calculated as if all the mass were located at the center of mass of the galaxy). Note that these particles need not be unbound from the greater dark matter potential well. Gas particles may be ejected multiple times in their history provided that they are identified as part of the disk in between ejection events.

While ejected gas particles need only become unbound from the baryonic disk, a subset of the ejected gas eventually also escapes the halo. Any gas particle that ends up beyond $R_{\rm vir}$ at a snapshot subsequent to ejection is identified as having been expelled from the halo.

In addition to the ejected gas, there is a larger population of gas particles that are labeled as part of the disk in one snapshot but not in a subsequent one. This occurs whenever a gas particle becomes too hot, too low in density, or too distant from the midplane of the galaxy. As such, it can include tidally stripped material, in addition to gas affected by feedback. Ejected gas particles, therefore, are a subsection of this broader category, just as the gas particles that are expelled from the halo are a subsection of the ejected gas.

These identifications of gas outflow and accretion are limited by the temporal spacing of the snapshots. For the simulations in this paper, snapshots were spaced approximately 100 Myr apart. Our time resolution for tracing inflows and outflows, therefore, is also about 100 Myr. Furthermore, the limited number of snapshots means that particles may have been ejected and reaccreted between two concurrent snapshots. In such a case, an outflow would not have been identified. This limited time resolution means that the outflowing and accretion rates must be considered lower limits. The similar snapshot spacing across simulations ensures, however, that we can draw a comparison across the different galaxies.

Figure 2 shows the cumulative mass-loss history for each of our simulated galaxies versus time since the big bang, as a fraction of the final virial mass (listed in the upper left). The dashed line shows the total baryonic mass in the disk as a fraction of the redshift zero halo mass. Merger events can be identified by the sudden jumps, more common in larger-mass halos and at earlier epochs.

The black line shows the cumulative gas mass accreted to the disk, including reaccretion events (stars are not included). The green line shows the cumulative outflow mass from the disk. While disk masses tend to stabilize at later epochs, the total mass loss generally increases roughly linearly with time, mimicking the accreted mass. According to these accretion and outflow definitions, a roughly constant mass of gas enters and leaves the disks at late times. Also notable is the greater amounts of gas accretion and loss from the disk compared to the final virial mass in more massive galaxies. The smaller baryonic fraction of dwarf galaxies is the result of both lower accretion rates compared to their virial mass and the loss of a greater fraction of their accreted material, shown further in Section 3.2.

We further subdivide the cumulative mass loss into gas ejected from the disk (red) and gas that is expelled from the halo (blue). Since gas expelled from the halo is a subset of gas ejected from the disk, it is always lower, but the two generally track each other well. At late times much of the disk mass loss is not in "ejected" material (i.e., gas that becomes dynamically unbound from the disk). Rather, it is dominated by gas that escapes the disk but does not become dynamically unbound. This gas that is removed from the disk but not ejected includes material heated by SNe to above 10^4 K, gas that is tidally stripped, and gas that is entrained by outflowing gas.

3. RESULTS

3.1. Global Galaxy Properties

The balance between gas accretion, star formation, and outflows determines the baryonic content of galaxies. Therefore, the observed stellar and cold gas masses of galaxies act as a basic constraint on theoretical models. Our first step, therefore, is to verify our simulated galaxies' agreement with global $z = 0$ trends in the baryonic content of observed galaxies, in particular the stellar mass–halo mass, Tully–Fisher, and mass–metallicity relations.

The halos in our sample are shown to match the $z = 0$ stellar mass–halo mass relation inferred from abundance matching (Behroozi et al. 2013; Moster et al. 2013; Brook et al. 2014) in Figure 3. In order to make an accurate comparison, stellar masses were calculated from simulated photometric observations, while halo masses were taken from dark-matter-only simulations, as in Munshi et al. (2013). The agreement between the simulations and the abundance-matching models indicates that the simulated galaxies are able to form the correct mass of stars for their halo mass over the course of their lifetime. Note that calculating the stellar masses from photometric observations results in smaller masses than measuring them directly from the simulations (Munshi et al. 2013). For these galaxies the actual stellar masses (listed in Table 1) are about 1.3–1.4 times the photometrically determined ones.

Figure 4 compares the simulations to the observed baryonic Tully–Fisher relationship from McGaugh (2005) (the sum of the stellar and cold gas mass of galaxies as a function of their rotational velocities). To ensure a fair comparison to these data, we compute the baryonic mass as the sum of the stellar mass calculated from the galaxies' B-band magnitudes using a mass-to-light ratio determined by the B–V color following McGaugh (2005), together with the H I, H_2, and He I gas mass. Additionally, the asymptotic velocity, V_f, is calculated by fitting either an increasing or decreasing arctangent function to the circular velocities for radii that lay between twice the softening and less than the radius containing 90% of the cold gas. The agreement is excellent over the entire range of overlapping masses.

Analogously, Figure 5 shows the simulated galaxies along the observed SDSS i-band Tully–Fisher relation from Geha et al. (2006) and Pizagno et al. (2007). The Pizagno et al. (2007) data are for the tangental rotational velocities, while the data from Geha et al. (2006) employ the H I line width and thus should be interpreted as lower limits to the circular velocities. The simulated galaxies follow both the baryonic and standard Tully–Fisher relations across nearly an order of magnitude velocity range.

The Tully–Fisher plots confirm that the feedback mechanism in these simulations is able to solve the so-called angular momentum crisis in galaxies noted in early simulations without strong stellar-driven feedback (Navarro & Steinmetz 2000; Steinmetz & Navarro 1999). Feedback primarily solves this problem by the strong suppression of star formation in dwarf galaxies (Munshi et al. 2013). As a result of this suppression,

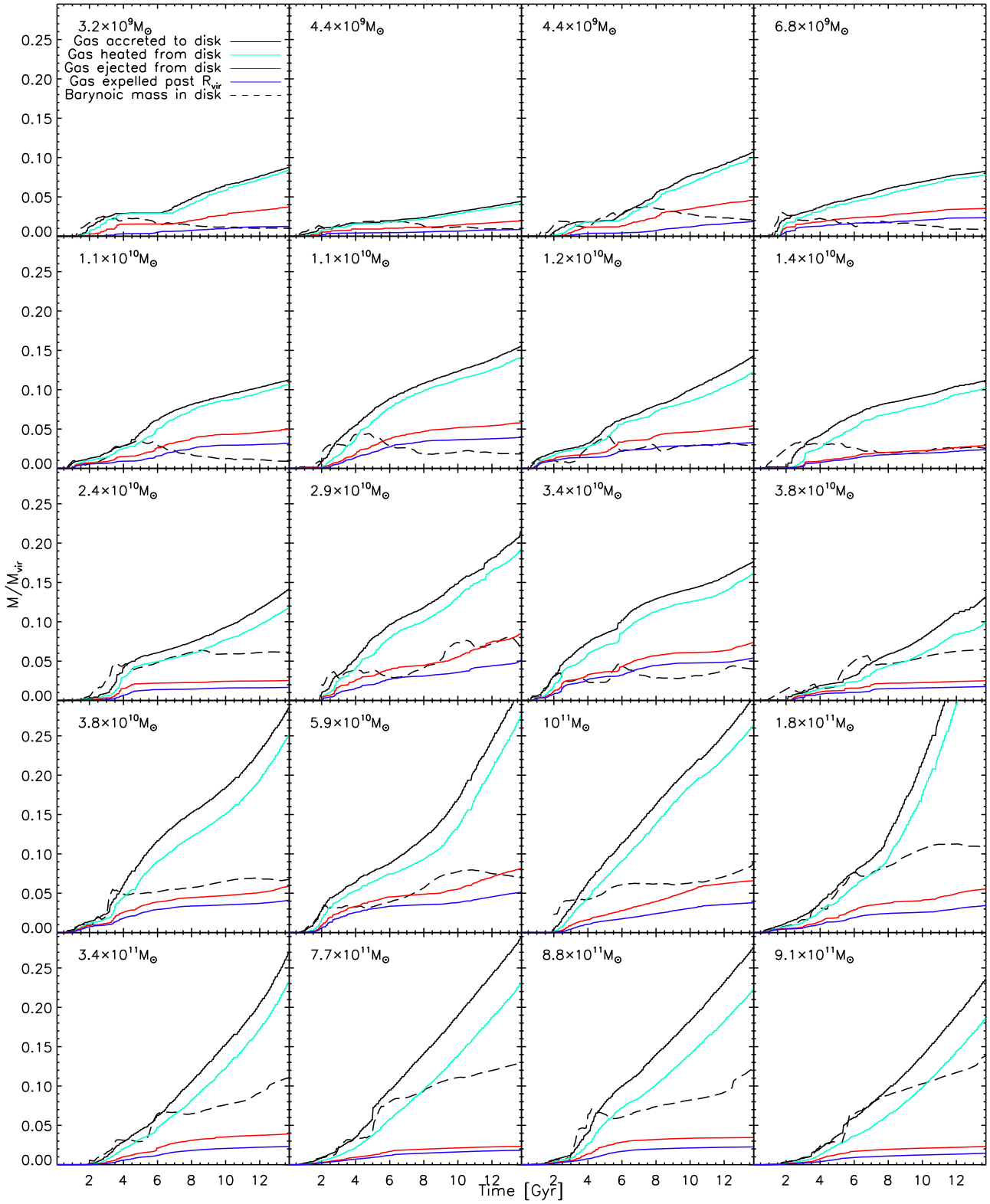

Figure 2. Cumulative mass-loss history for each of the galaxies. In these figures, the mass loss is scaled by the final virial mass of the galaxies. The solid black line indicates the total cumulative mass of gas particles accreted onto the disk of the galaxy, including any reaccretions of the same particle. The colored solid lines show the cumulative mass of gas particles ever removed from the disk (green), ejected such that they become dynamically unbound from the disk (red) and expelled beyond the virial radius (blue). For comparison, the dashed lines show the total baryonic mass within the disk. Occasionally the dashed line (total disk baryon mass) lies above the black solid line (cumulative mass of accreted gas) because of stellar accretion.

there is less growth via merging that would otherwise generate an overly peaked central rotation curve (Governato et al. 2009). Additionally, as will be further discussed in Section 3.7, these outflows reduce the amount of material in the centers of galaxies through the preferential removal of low angular momentum gas. As noted by Brook et al. (2012a), outflows

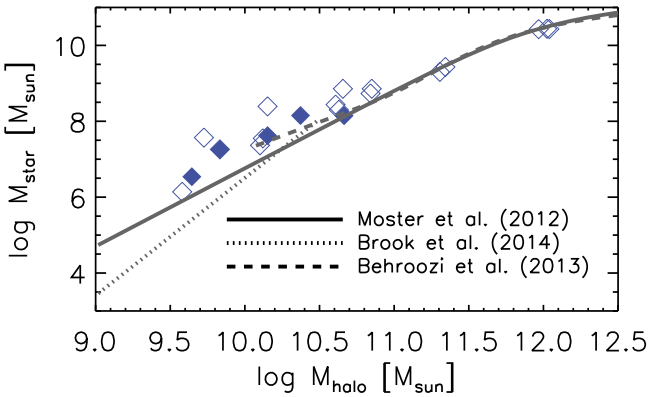

Figure 3. Redshift zero stellar mass–halo mass relation for the simulated galaxies (blue diamonds), compared to abundance-matching-derived fits from Behroozi et al. (2013), Moster et al. (2013), and Brook et al. (2014) (gray lines). Filled diamonds represent high-resolution ($\epsilon = 85$ pc) simulations, while open diamonds represent the medium-resolution ($\epsilon = 170$ pc) simulations. In order to better mimic the observations, stellar masses were determined from mock-photometric observations and halo masses were taken from dark-matter-only simulations.

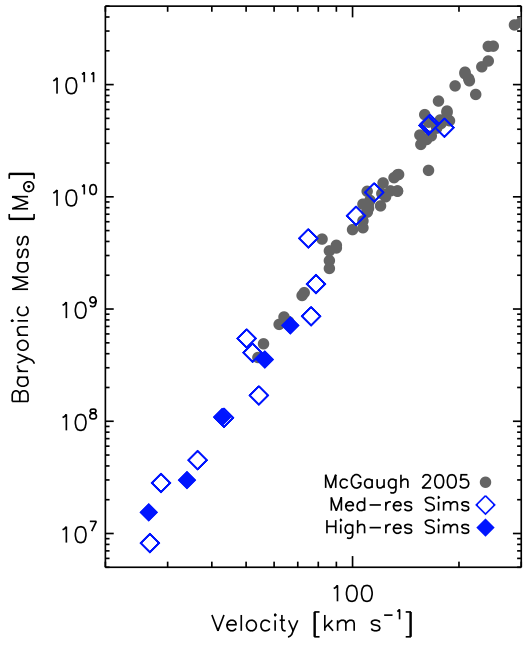

Figure 4. Baryonic Tully–Fisher relation for the simulated galaxies (blue diamonds), compared to observed galaxies from McGaugh (2005) (gray circles). Filled diamonds represent high-resolution ($\epsilon = 85$ pc) simulations, while open diamonds represent the medium-resolution ($\epsilon = 170$ pc) simulations. As in the observations, the total baryon mass of the simulated galaxies was calculated from the H I, H_2, and He I gas masses and the photometrically determined stellar mass. The simulated galaxies lie along the same line as the observed galaxies, indicating that their baryonic masses scale appropriately with their rotational velocities.

play a key role in setting the angular momentum distribution in galaxies, and the agreement with the baryonic and *i*-band Tully–Fisher relation suggests that the outflows in these simulations are plausible.

The gas-phase metallicities of galaxies are controlled by the balance between the accretion of pristine gas, the injection of metals into the ISM from stars, the ejection of metal-enriched ISM gas by feedback, and the reaccretion of enriched gas (e.g., Finlator & Davé 2008; Peeples & Shankar 2011; Davé et al. 2012).

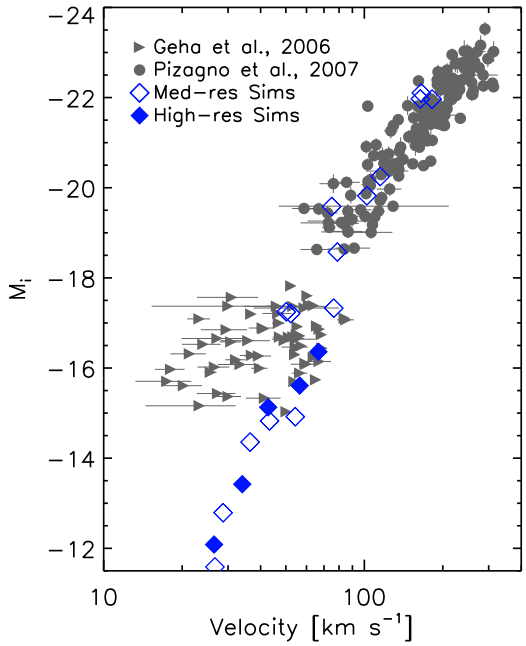

Figure 5. The *i*-band Tully–Fisher relation for the simulated galaxies (blue diamonds) compared to observed galaxies from Pizagno et al. (2007) and Geha et al. (2006) (filled gray circles and triangles, respectively). Filled diamonds show the high-resolution simulations, while open diamonds show the medium-resolution runs. While the Pizagno et al. (2007) data are of the tangental rotational velocities, the data from Geha et al. (2006) are of H I line widths. Therefore, when comparing to the simulated galaxies, the data from Geha et al. (2006) should be considered lower limits on the actual tangental rotational velocities. In general, the simulated galaxies follow the observed Tully–Fisher relation across nearly an order of magnitude in velocity.

Despite the complexity of the processes, galaxies follow a well-defined mass–metallicity relationship (Tremonti et al. 2004), albeit subject to calibration uncertainties in metallicity indicators (Kewley & Ellison 2008). Thus, the mass–metallicity relationship provides another strong test of the plausibility of our outflow model. Previously, Brooks et al. (2007) found that galaxies generated using an earlier version of GASOLINE follow the observed mass–metallicity relationship. Here we update that analysis to verify our sample of simulated galaxies with the current ISM model and star formation and feedback parameters.

Figure 6 shows our simulated galaxies in relation to the observed redshift zero mass–metallicity relationship from Lee et al. (2006), Tremonti et al. (2004), and Andrews & Martini (2013).[12] The Tremonti et al. (2004) metallicity data were lowered by 0.26 dex in order to account for the offset in the metallicity calibration, as noted by Erb et al. (2006). Following Lee et al. (2006), stellar masses for the simulations are calculated from the *K*- and *B*-band magnitudes. Gas particle oxygen abundances are weighted by the particle's star formation rate (i.e., probability of star formation) to mimic the measurement of metallicities in star-forming regions for observed galaxies. The simulated galaxies with stellar masses between 10^8 and $10^9\,M_\odot$ have somewhat lower metallicites than the observed galaxies. Nevertheless, the simulated galaxies broadly follow a power law with $[O/H] \propto M_*^{0.3}$ in

[12] Note that the method used in Andrews & Martini (2013) differs from that of the other two observed samples. In Andrews & Martini (2013), the direct method was used to measure the metallicity from stacked spectra of SDSS galaxies, whereas in Lee et al. (2006) and Tremonti et al. (2004) metallicities were measured from the flux ratios of strong lines for individual galaxies.

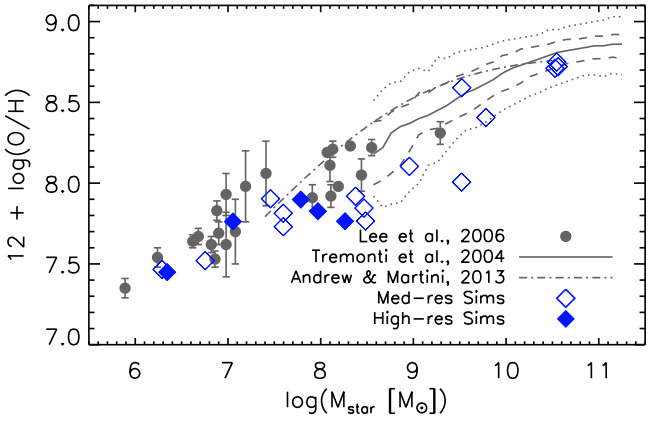

Figure 6. Mass–metallicity relation for the simulated galaxies (blue diamonds) compared to observed galaxies. Here the stellar masses of the simulations were calculated from mock-photometric observations. Filled diamonds represent higher-resolution simulations than the open diamonds. Gray circles represent individual observed galaxies from Lee et al. (2006). Lines show fits from Andrews & Martini (2013) (dot-dashed line) and Tremonti et al. (2004) (the solid line is the median of the galaxies in bins of 0.1 dex in stellar mass, the dashed line is the contour enclosing 68% of the galaxies, and the dotted line is the contour enclosing 95% of the galaxies). All lines from Tremonti et al. (2004) were shifted down by 0.26 dex, as the method used in that paper produces systematically higher oxygen abundances (Erb et al. 2006).

the range $M_* \approx 10^{6.5}$–$10^{10.5}\,M_\odot$, which is in good agreement with the observed galaxies over that wide range of masses.

Taken together, the stellar mass–halo mass, Tully–Fisher, and mass–metallicity relations provide stringent constraints on the cumulative effects of gas inflows, gas outflows, and star formation. The agreement of the simulations with these relations implies that such processes and their scalings with mass are plausibly represented in our simulations. We note that while the energy per SN (dESN) and star formation efficiency (c^*) were adjusted together to match the stellar mass–halo mass relation, no other tuning was done. Furthermore, the agreement between the medium- and high-resolution runs suggests that our results are not strongly dependent on numerical resolution, with the caveat that we only probe a factor of two in spatial resolution. In the remainder of this paper, we examine how the properties of the outflows themselves scale with halo mass.

3.2. Baryon Fractions in the Disk and Halo

The fraction of halo baryons in stars varies strongly with halo mass. Dwarf galaxies are known to be considerably less efficient than L^* galaxies at forming stars, i.e., the mass fraction of the expected halo baryon content of dwarf galaxies in the form of stars is much smaller than for L^* galaxies. The reason for this must be some combination of three factors: *preventive feedback*, where baryons are prevented from accreting either onto the halo or onto the disk from the halo; *ejective feedback*, where material enters into the disk but is ejected back into the surrounding halo or beyond; and lower *global star formation efficiency*, in which gas enters and remains in the disk but is less efficient at forming stars. In this section we quantify the relative importance of these processes for simulated galaxies.

The top panel of Figure 7 shows the redshift zero baryonic fraction of our simulated galaxies as a function of the expected cosmic halo baryon mass (i.e., the baryon fraction, f_b, times the halo mass). The filled red squares show the $z = 0$ fraction of baryons in the disk (cold gas plus stars), while the filled blue diamonds show the fraction of baryons in the halo. The

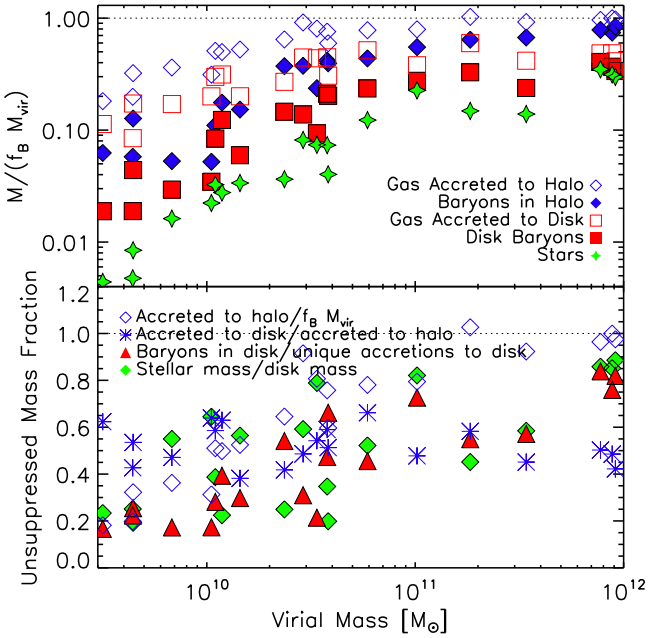

Figure 7. Top: fraction of the virial mass scaled by the cosmic baryon faction in different components of the galaxy. In addition to showing the instantaneous galaxy properties at $z = 0$ (filled symbols), this plot indicates the total mass ever accreted into different components of the galaxy (open symbols). Blue diamonds represent all baryons ever accreted onto the halo (open blue diamonds) and baryons currently within the halo (filled blue diamonds). Red squares represent all the baryons ever accreted onto the disk (open red squares) and all baryons currently part of the disk (filled red squares) in the form of cold, dense gas ($\rho \geqslant 0.1$ amu/cc and $T \leqslant 1.2 \times 10^4$) or stars. Green stars represent the present stellar mass, with values taken directly from the simulation. Bottom: relative efficiency of various methods at suppressing star formation. Blue diamonds show the fraction of the cosmic baryons accreted to the halo, an indication of the importance of halo preventative feedback, while blue asterisks show the fraction of halo gas accreted onto the disk, a result of disk preventative feedback. Red triangles show the fraction of baryons accreted to the disk that are still there at present day, which is a function of the ejective feedback. Green diamonds (mass fraction of the disk in the form of stars) show the relative efficiencies of the galaxies in forming stars.

corresponding open symbols show the total mass ever accreted into each component since a redshift of 3 (counting a given particle only once, even if accreted multiple times). Finally, the green stars indicate the present stellar baryon fraction.

The bottom panel of Figure 7 further summarizes the relative importance of preventative feedback, ejective feedback, and lower global star formation efficiencies in suppressing star formation. In this panel, the fraction of the expected baryonic halo content that is accreted onto the halo is shown by blue diamonds, and the fraction of halo gas accreted onto the disk is shown by blue asterisks. The fraction of accreted baryons that remain in the disk at $z = 0$ is shown by red triangles, and the stellar fraction of the disk is shown by green diamonds. As can be seen from the top panel of Figure 7, all baryon fractions increase with halo mass. The stellar baryonic fraction goes from $\lesssim$1% for $M_{\rm halo} \lesssim 10^{10}\,M_\odot$ to about 20% for L^* halos.

Preventive feedback manifests in two distinct forms in the plot, as shown by the open symbols in the top panel. The first is halo preventive feedback, in which the halo never receives its cosmic share of baryons. This is seen as the difference between the dotted line at unity and the open blue symbols. Next is disk preventive feedback, whereby the disk does not receive all the baryons accreted onto the halo. This is quantified by the

difference between the open blue symbols and open red symbols.

Addressing first halo preventative feedback, at virial masses below a few times $10^{10}\,M_{\odot}$ the halos have reduced amounts of material ever accreted onto the halo. This halo preventative feedback is also evident in the bottom panel, where the open blue diamonds mark the fraction of the expected baryonic content ever accreted to the halo. The existence of halo preventative feedback for virial masses less than a couple times $10^{10}\,M_{\odot}$ is expected from the impact of the cosmic UV background, which reduces baryon fractions for galaxies with $M_{\rm vir} \lesssim 10^{9.8}\,M_{\odot}$ (Gnedin 2000; Hoeft et al. 2006; Okamoto et al. 2008). There is some uncertainty in this so-called filtering mass, so potentially our simulations are consistent with simple photoionization suppression, especially since only gas that was in the galaxy at $z = 3$ or later is included. However, a distinct effect could owe to some other form of preventive feedback (e.g., Mo & Mao 2002) such as heating by wind energy (Oppenheimer et al. 2010; van de Voort et al. 2011). At halo masses $\gtrsim 3 \times 10^{10}\,M_{\odot}$, halos generally accrete their fair share of baryons.

Disk preventive feedback, seen by the difference between the open blue diamonds and open red squares in the top panel and the blue asterisks in the bottom panel, is typically around a factor of two. This has only a mild dependence on halo mass, indicating that once baryons are inside the halo, an approximately uniform fraction of them reach the disk. This trend clearly cannot be extrapolated to masses above those considered here, since halos well above $10^{12}\,M_{\odot}$ generally have substantial hot gaseous halos but have little gas in their disks (and typically do not have disks at all). These simulations are also missing possible sources of preventative feedback, namely, heating from active galactic nuclei and ionizing radiation from the galaxies' stars, that could possibly introduce a mass trend within star-forming galaxies (Kannan et al. 2014). Nevertheless, our simulations here indicate that disk preventive feedback is not strongly dependent on halo mass.

We now consider ejective feedback, which can be seen as the difference between the open and filled points of the same color in the top panel. For instance, the halo has accreted a baryon fraction indicated by the open blue diamonds, but currently only contains the fraction indicated by the filled blue diamonds, so the difference must have been ejected from the halo. Similarly, the difference between the open and filled red squares quantifies disk ejection. Disk ejection is also apparent from the red triangles in the bottom panel, which mark the fraction of mass accreted to the disk that remains in the disk at $z = 0$.

In our simulations, there is only one energetic process included that can counteract gravity, eject material, and produce galactic winds, namely, SN feedback. Hence, ejective feedback quantifies how much material SN feedback has removed from the disk and the halo. Note that this does not necessarily mean that all ejection consists of gas directly heated by the SN, as there could be some entrainment, pushing, or heating of the surrounding gas. Ultimately, though, the energy source must have been the SNe. As can be seen from the figure, ejective processes have a strong dependence on halo mass. Low-mass disks can eject the vast majority of accreted material, whereas for L^{*} galaxies the disk ejection is much less. We further explore this mass dependency in Section 3.4.

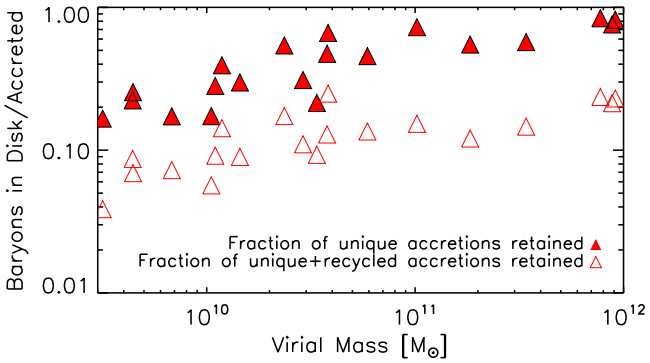

Figure 8. Mass of disk baryons at redshift zero as a fraction of the total mass accreted onto the disk. For the filled triangles, the denominator is the total mass of unique gas particles accreted. For the open triangles, the denominator includes multiple accretions of the same gas particle. According to both definitions, the fraction of accreted baryons retained in the disk increases by about a factor of four across the halo range covered.

Finally, we consider the global star formation efficiency, which is quantified by the difference between the filled red squares and the green stars in the top panel and by the green diamonds in the bottom panel. Again, this shows a significant trend with halo mass, such that low-mass galaxies are less efficient at turning their disk baryons into stars. In observed galaxies this lower global star formation efficiency is evident in the higher gas fractions of dwarf galaxies. The reason is a combination of at least two effects. The first is that low-mass galaxies tend to be more diffuse, with the lowest-mass systems often being bulgeless and irregular, and hence the star formation rate, which is superlinearly dependent on the local density, is reduced for a given amount of mass. Second, low-mass galaxies have lower metallicity, which reduces the amount of dust shielding, and consequentially, the H_2 fraction. As a result, the dwarf galaxies have lower rates of conversion of disk gas into stars. Overall, inefficiency in global star formation seems to be of comparable strength to ejective effects across all masses.

So far we have only considered unique accretion events, which specifically neglects recycling of previously ejected material back into the disk. To examine this, we compare the disk baryon fractions relative to the total accreted and reaccreted fraction onto the disk in Figure 8. In the case of the filled red triangles, we consider only unique accretions (i.e., not including recycling); this is equivalent to the red triangles in the bottom panel of Figure 7. In the case of the open red triangles, however, we consider all accretions, including recycled material.

Several trends are evident. First, the fraction of both unique and total accreted mass that ends up in the disk has a strong dependence on halo mass. In the highest-mass galaxies about 80% of the baryons that are accreted once ended up in the disk, while in the lowest-mass ones it is $\sim$4$\times$ smaller. The *total* accretion, in all cases, is also about 4$\times$ smaller for unique events than for reaccreted events. That is, typically there is 3$\times$ greater recycled accretion than first-time accretion. This number is roughly independent of mass, showing that the amount of recycling relative to first-time accretion is not strongly mass dependent. We explore this topic in greater depth in Section 3.6.

3.3. Quantifying Ejected Material

We now examine in more detail the role of ejective feedback in regulating the baryonic content for galaxies of different masses. Specifically, we quantify the mass of outflows that galaxies experience as a function of their virial mass. We quantify outflows in several ways: (1) the gas that becomes too hot or rarified to be considered part of the disk; (2) the gas that becomes energetic enough to dynamically escape the baryonic disk ("ejected"); and (3) the gas not only ejected from the disk but also expelled from the entire halo. Each of the latter categories is a subset of the former. We can also subdivide any one of those categories between the gas particles that directly had SN energy transferred to them and those that were entrained by other affected gas. Note that, with regard to Figure 8, all the outflow masses should be compared to the total accretion including recycling as opposed to unique accretion, since outflows also must eject recycled material.

The top panel of Figure 9 shows the total amounts of gas ejected from the disk (red squares) and expelled from the halo (blue diamonds) since a redshift of 3 as a function of the virial mass. For comparison, the mass in stars formed over the history of the galaxy is also shown (green stars). For galaxies with $M_{\rm halo} \lesssim 10^{11}\,M_{\odot}$ the amount of ejected material exceeds the stellar mass, and at the lowest masses it does so by an order of magnitude. This leads to the conclusion that, particularly for smaller halos, the visually dominant stellar component is merely a "trace" amount of mass leftover from the small imbalance between accretion and outflows.

The middle panel of Figure 9 quantifies the mass loss more precisely via the *effective mass loading factor* $\tilde{\eta}$, defined as the amount of mass driven out by feedback relative to the amount of stellar mass formed. This is different from the more canonical mass loading factor η, which is the instantaneous mass-loss rate relative to the current star formation rate. The effective mass loading factor is in some sense a time average of η over a galaxy's life. We note that, owing to our limited snapshot time resolution of ∼100 Myr, $\tilde{\eta}$ is actually a lower limit on the true value, since there could be recycling happening on smaller timescales that would add to the total outflow mass.

The effective mass loading factor, $\tilde{\eta}$, displays the trends expected from the top panel. For our most massive halos, $\tilde{\eta}$ (for material either ejected from the disk or expelled beyond the virial radius) is comparable to or less than unity, showing that galaxies retain in stars roughly as much material as they expel. At small masses, however, $\tilde{\eta}$ for ejected material can reach up to ∼30, and for the subset of the ejecta that is expelled beyond the virial radius, $\tilde{\eta} \sim 10$. This relationship demonstrates the extent to which less massive galaxies are more efficient at removing material from the galaxy through stellar feedback; we will quantify this further in the next section.

We also show the total mass of gas heated by feedback relative to the stellar mass as the green circles. Such gas is heated enough to no longer be considered part of the atomic and molecular ISM but may never have enough kinetic energy to be considered "ejected" from the disk. Therefore, this group includes gas that is briefly heated by SNe but quickly cools back onto the disk. This comprises a significant amount of material and shows the impact SNe can have on the gas available for star formation, even when not removing the gas from the disk for great lengths of time.

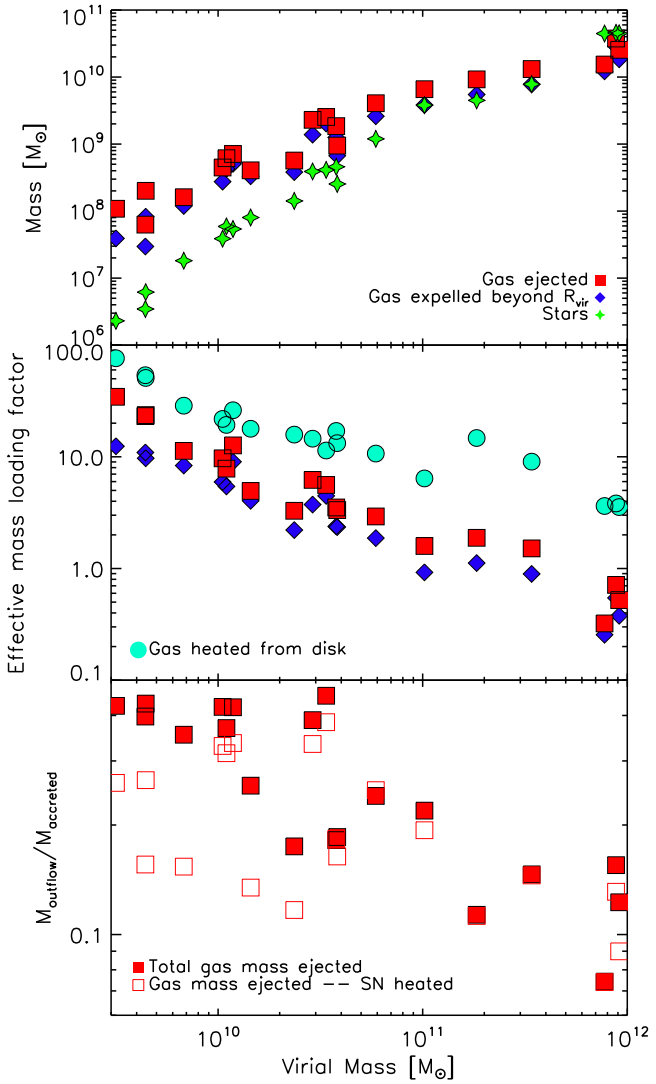

Figure 9. In all plots, red squares represent the gas ejected from the disk. Top: total gas mass ejected over the histories of the galaxies as a function of their virial mass. Here the mass of ejected gas that eventually crosses the virial radius (blue diamonds) and the stellar mass of the galaxies (green stars) are shown for comparison. The mass of the outflows is significant compared to the stellar mass and increases with galaxy mass. Middle: total outflow mass divided by the stellar mass formed over the histories of the galaxies (the effective mass loading factor) as a function of the galaxy's redshift zero virial mass. In addition to the gas ejected from the disk or expelled beyond the virial radius (blue diamonds), we also show all the gas that became too hot or rarefied to be considered part of the disk (filled green circles). The effective mass loading factors display strong power-law dependencies with mass. Bottom: mass fraction of gas ever accreted onto the disk of the galaxy that is ejected from the galaxy. Open squares show the ejected gas particles that SN energy was directly transferred to during the simulation, as opposed to gas particles that were entrained. As predicted from the lower baryon fractions of dwarf galaxies, higher fractions of gas accreted onto the disk are later ejected from less massive galaxies. Lower-mass galaxies also lose greater fractions of their gas through entrainment rather than direct heating.

At large masses, most of the disk baryons are in stars, and so $\tilde{\eta}$ approximately reflects the amount of ejection relative to the disk baryons. But at small masses this is not true, because the lower star formation efficiency results in large gas reservoirs that far exceed the stellar component. Hence, a third quantitative view of outflows is to compare the outflow mass to the total amount of baryons ever accreted onto the disk.

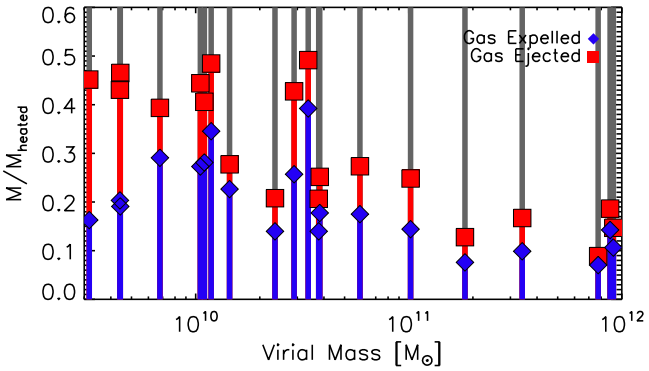

Figure 10. Fraction of gas heated sufficiently to be removed from the disk ($M_{\rm heated}$) that was either ejected from the disk (red) or expelled beyond the virial radius (blue). The fraction of $M_{\rm heated}$ that is ejected strongly decreases with virial mass. This trend can be accounted for by the relatively larger disk masses in more massive halos. The fraction of $M_{\rm heated}$ that is expelled from the halo shows a similar but far weaker trend with mass. Also evident is the decreasing fraction of ejected particles later expelled from the halo.

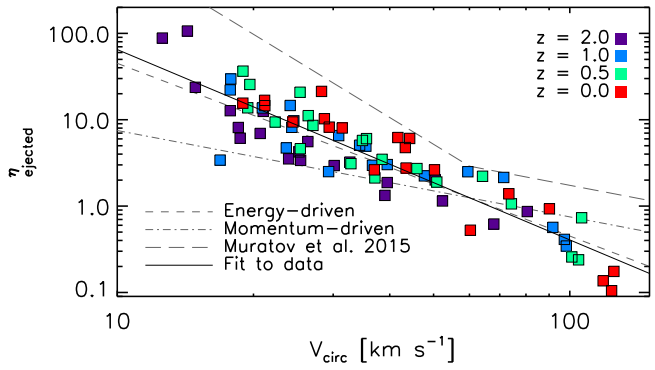

Figure 11. Total gas mass ejected divided by the stellar mass formed within 1 Gyr time bins as a function of halo circular mass. The mass loading factors at different redshifts are indicated by different color points. A power-law fit to all the data points, shown as the black line, results in an exponent of −2.2. For comparison, the dashed and dot-dashed lines show an energy-driven scaling ($v_{\rm circ}^{-2}$) and a momentum-driven scaling ($v_{\rm circ}^{-1}$), respectively (normalized to the data at $v_{\rm circ} = 60$ km s^{-1}). Additionally, the redshift zero fit to the mass loading factor given in Muratov et al. (2015) is included as a long-dashed line. Note that differences between how the ejecta was selected here and in Muratov et al. (2015) can account for differences in the offset but not in the scaling.

The bottom panel of Figure 9 shows the fraction of ejected material relative to the total accreted mass (including recycled accretion). The open squares show the ejected material that was directly heated by SNe, while the filled squares show the total amount of ejected material. As can be anticipated from the reduced baryonic fraction of dwarf galaxies, higher fractions of accreted material are lost as the virial mass decreases. However, the trend is not as strong or as clean as those for $\tilde{\eta}$ because the lower star formation efficiencies of lower-mass galaxies result in much of the accretion going into the gas reservoir rather than being ejected.

The effect of entrainment can be seen by comparing the open and filled symbols in the bottom panel. At high masses, there is little entrainment; most of the gas particles either ejected or expelled had energy transferred to them directly from SNe at some point in their history. In contrast, there is substantial entrainment of gas in dwarf galaxies, in some cases as much as doubling the mass of the SN-heated material.

In order to better analyze the division between all gas that was heated by SNe and the subsection that was ejected from the disk or expelled beyond the virial radius, we show the relative fractions of each for the different halo masses in Figure 10. In this figure each gray bar represents the total mass of gas that became too hot or rarefied to be considered part of the disk (corresponding to the green circles in the middle panel of Figure 9), while the red shows the fraction of that gas that was ejected from the disk and the blue the fraction that was expelled beyond the virial radius. The fraction of the heated gas that was ejected (and, to a lesser extent, expelled beyond the virial radius) decreases with increasing halo mass. This trend demonstrates the greater difficulty in gas becoming energetic enough to dynamically leave the disk or halo of more massive galaxies. Furthermore, the fraction of ejected particles that were later expelled beyond the virial radius also decreases with halo mass. In the lowest-mass galaxies less than half of the ejected gas eventually leaves the halo, whereas in the higher-mass galaxies almost all of the ejected gas does. This trend in the fraction of ejected gas later expelled from the halo is the result of the relatively larger disks in more massive halos—the larger mass the disk is relative to the halo, the more likely it is that a particle that becomes dynamically unbound from the disk will exit the halo.

3.4. Mass Loading Factor Evolution

We now examine the mass loading factor, η, as a function of redshift and halo mass. We obtain a more "instantaneous" mass loading factor by taking the total mass lost only in the past gigayear at any given redshift and comparing it to the mass of stars formed over the same time period. While this is not truly instantaneous, it allows us to examine how this quantity has varied with cosmic time. We also examine η as a function of circular velocity, as that is more straightforwardly relatable to recent models of the physics of outflow driving. In this case, "circular velocity" refers to the circular velocity calculated at the virial radius from the total halo mass.

Figure 11 shows the mass loading factors for the ejected material at four different redshifts, against the corresponding circular velocities at those redshifts. There is no discernible trend with redshift in either shape or amplitude. Fitting all the values together, we obtain a power-law fit of $\eta = \eta_0 v_{\rm circ}^{-2.2}$ for ejected material, roughly consistent with energy-driven winds (Chevalier & Clegg 1985).

Cosmological simulations often have to assume a mass loading factor since they lack the resolution to directly generate outflows. The energy-driven scalings we predict are consistent with those assumed in state-of-the-art simulations that match observed properties of galaxies and the CGM (Dave et al. 2013; Ford et al. 2014; Genel et al. 2014; Vogelsberger et al. 2014). They are, however, somewhat different from that predicted by the Feedback in Realistic Galaxies (FIRE) suite of zoom simulations that also self-consistently drive outflows; the FIRE simulations find a shallower dependence for $v_{\rm circ} > 60$ km s^{-1} and a steeper dependence for smaller systems (Muratov et al. 2015). The amplitude is somewhat lower than typically assumed in cosmological runs; we predict that η is unity for $v_{\rm circ} \approx 100$ km s^{-1} (i.e., $M_{\rm halo} \sim 10^{11}\,M_\odot$), whereas such simulations typically assume unity mass loading at $M_{\rm halo} \sim 10^{12}\,M_\odot$, corresponding to mass loading factors a factor of two smaller than typically assumed (e.g., Dave et al. 2013). However, these mass loading factors are only calculated for the outflowing gas that is sufficiently energetic to be classified as "ejected." If all the gas identified as leaving the

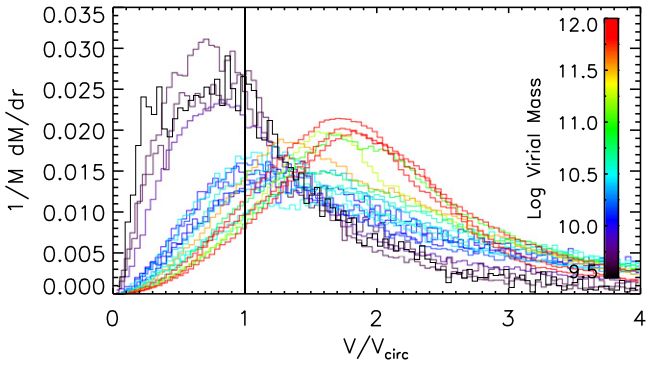

Figure 12. Normalized distribution of the velocities of the ejected material for individual galaxies. The highest-mass galaxies are shown in red, whereas the lowest-mass galaxies are shown in purple. The velocities of the ejected material were determined at the step immediately following their removal from the disk. The velocities of the ejected material are then scaled by the circular velocity defined for the halo potential at the time when the particle was ejected.

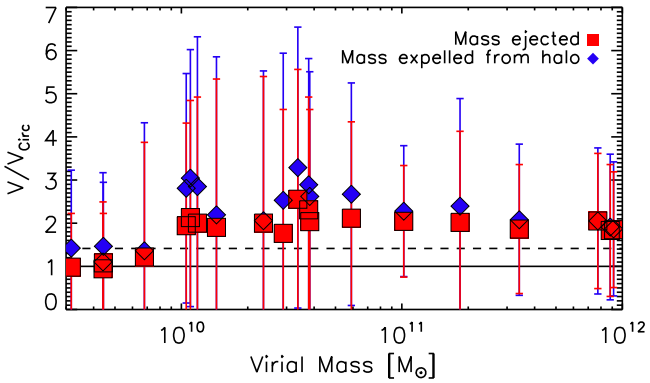

Figure 13. Velocities of ejected and expelled material. The median velocity of the material at the step immediately after ejection from the disk is shown as a function of virial mass. These velocities are normalized by the circular velocity of the halo at the time of ejection. This plot shows both the total ejected gas (red squares) and the subsection of that gas that is later expelled (blue diamonds). The solid line marks the velocity equal to the circular velocity, while the dashed line marks the escape velocity of the halo.

disk is included, the scaling of the mass loading increases to values closer to those assumed in most cosmological simulations.

3.5. Velocities of Outflows

Outflow velocities are generally observed to be proportional to the circular velocity (Martin 2005; Weiner et al. 2009; though see Steidel et al. 2010), and cosmological simulations that employ kinetic feedback typically assume such a scaling. Because our blastwave feedback depends on the local density and pressure, affected particles show a distribution of energies, temperatures, and velocities. We can thus compare these self-consistently generated velocities to those observed and employed in other models.

Figure 12 shows the distribution of the velocities of ejected gas particles in the snapshot following their removal from the disk scaled by the circular velocity of the galaxy at the time of the outflow. Because of the spacing between snapshots (100 Myr), particles are typically already 0.04 $R_{\rm vir}$ from the center of the galaxy when their velocity is measured. As such, particles may have slowed down during the period of time between when they actually left and when they are identified as having done so. Nevertheless, this method allows us to make approximate measurements and to compare velocities across galaxies. As in Section 3.4, the circular velocity used here is the circular velocity calculated at the virial radius for the total mass of the halo. Other definitions of rotational velocity will produce different scalings. For instance, the asymptotic velocities, V_f, used for the baryonic Tully–Fisher relation (Figure 4), are about 1.4 times greater than the circular velocities for the halo mass range here. Normalizing the outflow velocities by V_f, therefore, would reduce the results shown by a factor of ∼0.7. For the most massive galaxies, the median outflow velocities are close to twice the circular velocity at the time of the outflow. For the least massive galaxies, in contrast, it is clearly smaller. This lower velocity of gas ejected from dwarf galaxies is consistent with their relatively smaller fractions of gas leaving the halo seen in Figure 10. Essentially, the relatively smaller disk-to-halo mass ratio of dwarf galaxies enables gas to be ejected at relatively smaller velocities. However, these smaller velocities are not necessarily sufficient for the ejected material to escape the halo.

Figure 13 quantifies the velocity trend with halo mass and circular velocity in more detail. Here we compare the median velocities of the ejected material and the subset of that material that later escapes the halo at the snapshot following their removal from the disk as a function of the redshift zero virial mass. Red points show the velocity of gas ejected from the disk, while blue points show the velocity of the subset of that gas that will end up expelled from the halo. The ejection velocity increases with halo mass, and median velocities are between 1 and 2.5 times the circular velocity for all halo masses. However, there is a huge range of velocities for any given galaxy, as indicated by the error bars. Taking a closer look, there is a noticeable trend that intermediate-mass galaxies have the highest relative outflow velocities. There is also a weak trend for material that later escapes the halo to have a higher velocity, but there is not a strong correlation between the velocity at the time step following when it exits the disk and its ability to escape the halo.

3.6. Wind Recycling

Previous theoretical work has shown that the recycling of gas through reaccretion back onto the disk is key to reproducing observed stellar masses (Oppenheimer et al. 2010; Henriques et al. 2013), metal enrichment (Davé et al. 2012), and mass distributions (Brook et al. 2012a). In this section, we quantify reaccretion, or wind recycling, as a function of halo mass, as well as the distribution of recycling times.

In Figure 14 we show the fraction of particles that has been reaccreted some number of times after being ejected from the disk. The number of times particles are reaccreted reveals the importance of gas recycling to the baryon content of galaxies and the mass of the disks. Across all galaxy masses, a significant fraction (20%–70%) of ejected mass is reaccreted onto the disk of the galaxy. There is possibly a slight mass trend toward more massive galaxies experiencing less reaccretion of their ejected material. As in the analysis of the fraction of ejected mass that later leaves the halo (Figure 10), such a trend is likely the result of the varying disk-to-halo ratio. Since the disk mass is a smaller fraction of the overall halo mass for

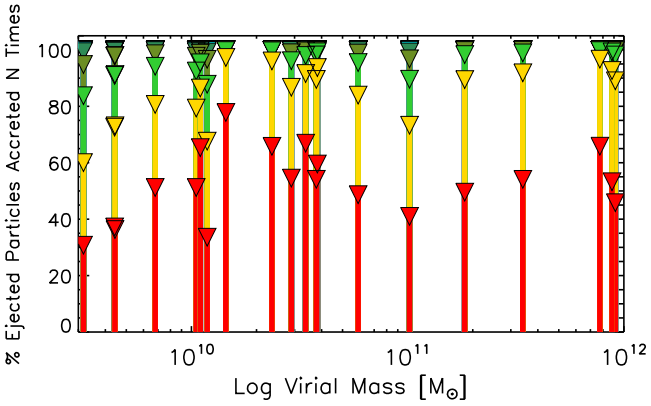

Figure 14. Mass fraction of gas ever ejected that was accreted some number of times onto the disk as a function of the virial mass. Each bar represents an individual galaxy. The red marks the fraction of ejected particles never reaccreted during the history of the galaxy. The yellow marks the fraction reaccreted once, the light green marks the fraction reaccreted twice, and so on. Between 20% and 70% of ejected material is later reaccreted.

dwarf galaxies, a greater fraction of the particles able to escape the disk potential are reaccreted because of the halo potential.

In contrast, we found no mass trend in the fraction of expelled material that is subsequently reaccreted. For all galaxies, only about 20% of the expelled material is reaccreted at least once. As this process is largely controlled by the growth of the halo (i.e., expelled particles can be reaccreted once the potential well is deeper), it is reasonable for it to be independent from halo mass within a hierarchical growth framework.

A key parameter discussed in current galaxy formation models is the recycling time, i.e., the amount of time ejected gas spends outside the disk prior to reaccretion. Cosmological simulations predict that the recycling time for momentum-driven wind scales roughly inversely with the halo mass for moderate-sized star-forming galaxies (Oppenheimer & Davé 2008; Oppenheimer et al. 2010), and some semianalytic models have found that similar scalings are best able to reproduce various observations, such as the stellar mass function (Henriques et al. 2013). Here we directly track the recycling time in our simulations as a function of halo mass.

Figure 15 shows cumulative histograms of the reaccretion timescales normalized by the total number of ejected particles. The recycling time distribution has a similar shape for all halos. Most gas particles are reaccreted on short timescales, with most reaccretion taking place over 500 Myr. Since our particle tracking is limited by our 100 Myr snapshot time resolution, we are unable to track particles that have recycling times less than 100 Myr; this fraction is likely not insubstantial. Conversely, the recycling time distribution also has a long tail, with some gas taking many gigayears to reaccrete.

In Figure 15, we also show the median and standard deviation of the reaccretion times as a function of virial mass. This shows a very weak halo mass dependence, roughly $t_{\rm rec} \propto M_{\rm halo}^{-0.1}$, with a typical reaccretion timescale of about 1 Gyr. This is in stark contrast to cosmological simulations and semianalytic models that seem to favor a strong halo mass dependence. Interestingly, the analytic equilibrium model of Mitra et al. (2015) finds an optimal fit to the stellar mass and halo mass, star formation rate, and metallicity from $0 < z < 2$ by assuming a recycling time with a weak halo mass

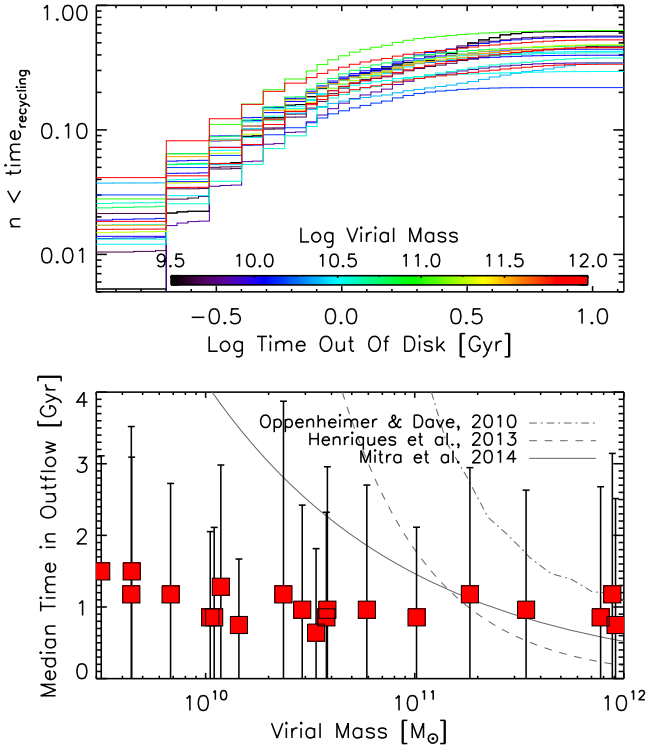

Figure 15. Amount of time before reaccretion of ejected particles to the disk. Top: normalized cumulative histogram of the amount of time particles spend between their ejection and subsequent reaccretion onto the disk. The colors represent the virial mass of the galaxies, with red being the highest-mass halos and purple being the lowest-mass halos. Where these lines asymptote indicates the total fraction of gas ever reaccreted. Bottom: median time for reaccretion of ejected particles as a function of halo mass, with the error bars representing the standard deviation. We find that on average particles take 1 Gyr to reaccrete and the recycling times have only a very weak dependency with halo mass. This result is in contrast to the halo mass dependency found by Oppenheimer et al. (2010) ($z = 0.5$ from the preferred "vzw" model), Henriques et al. (2013), and Mitra et al. (2015), shown here as the dot-dashed, dashed, and solid lines, respectively.

dependence of $t_{\rm rec} \propto M_{\rm halo}^{-0.45}$. This is still stronger than the dependence our simulations predict, but it is closer.

3.7. Ejecta Properties

Star-formation-driven outflows have been shown to have a strong effect on the angular momentum distribution of both baryons and dark matter (Brook et al. 2012a). Outflows preferentially remove low angular momentum central gas, and because of cloud–corona interactions, gas is reaccreted with higher angular momentum (Marasco et al. 2012). The effectiveness of this process depends on from where in the disk most outflow material is launched and to where it reaccretes. Here we examine these processes over a range of galaxy mass by tracking the location and angular momentum of particles at the time of ejection and reaccretion.

Figure 16 (top panel) shows the radius within which half of the ejected mass originated and is reaccreted as a function of halo mass. In our analysis, the originating radius is defined by the location of the gas particle at the snapshot immediately prior to being ejected and the reaccretion radius by the location of the gas particle at the snapshot following its reentry into the disk. Similarly, the half-mass radius of star formation is the radius within which half of the $z = 0$ stellar mass was formed,

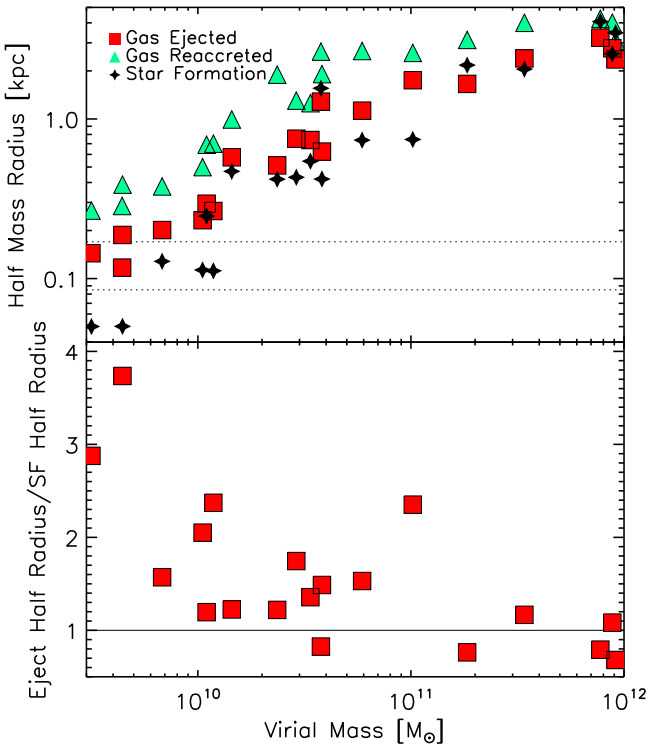

Figure 16. Source of the ejected material as a function of virial mass. The top panel shows the half-mass radius of the source of the ejected material (red squares), the reaccretion of the ejected material (green triangles), and the star formation (black stars). Here the half-mass radius is defined to be the radius from within which 50% of the ejected material originates or is reaccreted to or within which 50% of the star formation took place. The dotted horizontal lines mark the softening lengths for both resolutions of galaxies. The half-mass radii of the source of the ejecta, the location of reaccretion, and star formation increase with virial mass, as expected from the increasing size of the galaxies. For all galaxies, gas is reaccreted to a significantly larger area than it is ejected from. The bottom panel normalizes the half-mass radius of the ejected material by that of the star formation. The source of the ejected material roughly follows that of the star formation for galaxies above $10^{10}\,M_\odot$. For the four least massive galaxies, the half-mass radii of star formation are within the softening length (87 pc), which limits our ability to draw conclusions as to the relative locations of star formation and outflows in these galaxies. Nevertheless, it does appear that low-mass galaxies eject gas from a broader region compared to their star formation.

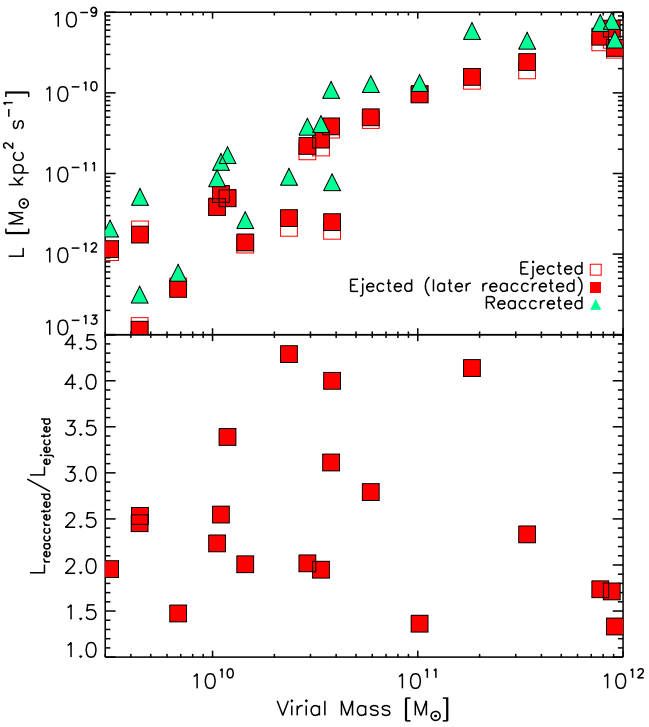

Figure 17. Median angular momentum of the ejected and reaccreted material as a function of virial mass. The top panel shows the median angular momentum of all the ejected material (red open squares) and the ejected material that is later reaccreted (red filled squares) at the snapshot immediately prior to it leaving the disk. Green triangles indicate the median angular momentum of the reaccreted material at the first snapshot after it reenters the disk. The bottom panel plots the ratio of the median angular momentum of the material after reaccretion to the median angular momentum of it prior to its ejection as a function of virial mass. On average, gas is reaccreted at significantly higher angular momenta, indicating that it is "spun up" in the halo.

which we obtain by tracking the location of each star particle at the time of creation.

Both the star formation radius and the ejection radius increase strongly with virial mass, roughly following a power law $R \propto M_{\rm halo}^{1/4}$, which is somewhat shallower than the halo virial scaling: $R \propto M_{\rm halo}^{1/3}$. This slight difference is consistent with the idea that lower-mass galaxies generally have a later Hubble type, are more extended, and have more angular momentum.

In the bottom panel of Figure 16, we normalized the half-mass radius of the ejected material by the half-mass radius of star formation. The resulting plot shows that the outflowing material roughly follows the star formation, as expected. There does appear to be a mass trend such that more massive galaxies have relatively more concentrated outflows. However, this trend is largely set by the four lowest-mass galaxies, whose star formation half-mass radii are within the softening length, so it is unclear how robust this trend is. Even for the more massive galaxies, though, the half-mass radius of ejected material is between 0.8 and 2.5 times the SF radius. From the typically greater half-mass radii of the ejecta, it is apparent that while the ejected material is centrally concentrated, it is somewhat more dispersed than the star formation.

Similarly, in Figure 17, we compare the median angular momentum of the ejected gas immediately prior to leaving the disk (open squares) to the median angular momentum of it immediately after reaccretion (green triangles). We also denote the subset of ejected gas that is later reaccreted by the filled red squares. There is little distinction between the angular momentum distribution of all the ejected material and the subset of that ejected material that is later reaccreted. Hence, material that recycles does not have a preferential initial angular momentum, which implies that it does not come from a preferred location in the disk. In contrast, it is clear that the reaccreted gas has significantly higher angular momentum at the time of reaccretion than it did when ejected.

In the bottom panel of Figure 17 we plot the ratio of angular momentum of the gas when reaccreted to that when ejected. This figure shows that ejected gas is reaccreted with higher angular momentum, typically increased by a factor of ∼2–3. There is a large scatter and no clear trend with mass, although the highest-mass galaxies all have fairly low "boosting" of the angular momentum; a larger sample will be necessary to see whether that is statistically significant. These results are consistent with previous work by Brook et al. (2012a) showing that ejected gas is "spun up" in the halo before reaccretion. It is qualitatively consistent with the redistribution of angular

momentum necessary to match observations of dwarf galaxy angular momenta by van den Bosch et al. (2001).

4. DISCUSSION

The blastwave feedback model used here is essentially a variation on the "energy-driven" wind scenario. In the energy-driven wind model, gas is driven from galaxies assuming that SN energy is conserved. This scenario is in contrast to the "momentum-driven" wind model (Murray et al. 2005), in which energy may be dissipated away but momentum is conserved. The difference between the blastwave feedback model and the analytic models for energy-driven winds applied to many cosmological simulations is that in the blastwave model the transfer of SN energy to the ISM is based on the local gas properties and is ignorant of the larger galaxy potential. Despite this key difference, the scaling for the mass loading factor as a function of $v_{\rm circ}$ is very close to the analytically derived scaling for energy-driven winds: $v_{\rm circ}^{-2.2}$ versus $v_{\rm circ}^{-2}$. We also found that the outflow velocity scalings determined for the sample of simulated galaxies follow the analytic solution for the energy-driven model. The median wind velocities of the ejected and expelled material had an approximately linear scaling with circular velocity. This is consistent with the analytic solution for energy-driven winds, namely, $v_w = 2\sigma\sqrt{f_L - 1}$ (Murray et al. 2005), where σ is the velocity dispersion and, therefore, proportional to the circular velocity.

The correspondence between analytic models and the blastwave feedback results implies that the relationship between mass loading and galaxy mass comes directly from the halo potential. Nevertheless, local gas properties *do* affect the efficiency of the energy transfer and, therefore, the scaling of the $v_{\rm circ}$–mass loading relationship. Christensen et al. (2014b) showed that the blastwave feedback model results in a much more efficient removal of gas when combined with a highly resolved ISM that included the cold molecular phase, as used here. This change in the efficiency is also apparent by comparing the results here to those in Woods et al. (2014), which examined a blastwave feedback model using lower-resolution simulations and without a molecular hydrogen model. In Woods et al. (2014), the blastwave feedback model was unable to remove baryons from $\approx 10^{12}\,M_\odot$ halos, whereas here 10%–20% of the gas accreted to halos in this mass range was removed by a redshift of zero (see Figure 7).

A somewhat remarkable aspect of the models shown here is that they are able to match the mass–metallicity relation despite having energy-driven wind scalings. In general, cosmological simulations that include energy-driven winds tend to produce a mass–metallicity relation that is too steep (Dave et al. 2013; Somerville et al. 2015). This may be because such simulations tend to rely solely on ejective feedback to suppress star formation at low masses (above the filtering mass). The simulations presented here, though, show that there is significant preventive feedback, even above the filtering mass, along with a mass-dependent star formation efficiency. For example, the fraction of halo gas accreted onto the disk is largely independent of halo mass over this sample of galaxies (see Figure 7), indicating that the suppression of halo gas accretion onto the disk is similar between dwarf and L^* galaxies. This preventative feedback can reduce the star formation in low-mass galaxies. It does not, however, have a strong impact on the gas-phase metallicity because that is determined by a competition between the accretion of fresh gas and the creation of new metals from stars (e.g., Finlator & Davé 2008). Hence, it appears that to simultaneously match the stellar mass function (or almost equivalently, the stellar mass–halo mass relation) and the mass–metallicity relation requires having significant preventive feedback across all mass scales, not just at high masses when active galactic nucleus feedback putatively happens. In our simulations, this may happen owing to wind energy that retards inflow into the disk, as also seen by van de Voort et al. (2011).

The energy-driven scaling determined in this suite of galaxy simulations follows the general convergence within the community toward energy-driven scalings at lower halo masses (Ford et al. 2014; Vogelsberger et al. 2014). It should be noted that our model does not include a prescription for different forms of early stellar feedback, such as radiation pressure, which are generally more consistent with a momentum-driven wind scenario.

Different models of early stellar feedback have been incorporated into a variety of galaxy formation codes (Stinson et al. 2012; Aumer et al. 2013; Ceverino et al. 2014; Hopkins et al. 2014), and they have been remarkable for their ability to reduce early star formation and to produce galaxies that match the high-redshift stellar mass–halo mass relation (Agertz & Kravtsov 2014; Wang et al. 2015). While very similar versions of the code used here have been shown to produce dwarf galaxies with star formation histories consistent with those observed from resolved stellar populations of local dwarf galaxies (Shen et al. 2014), the larger galaxies likely have too much early star formation (Christensen et al. 2014a). This potential discrepancy suggests that a combination of energy-driven and momentum-driven wind may yet be necessary to increase outflows sufficiently in higher-density gas to produce realistic star formation histories. An alternative to the addition of early stellar feedback exists, however, in improved modeling of SN feedback from clusters of young stars. Keller et al. (2014) describe such a parameter-free, resolution-independent SN feedback model. Similarly to early stellar feedback models, this model is able to reduce star formation before $z = 2$ and to produce a Milky-Way-mass galaxy with low bulge-to-total mass ratio (Keller et al. 2015).

In addition to affecting the removal of gas, the numerics of the simulation may affect the rates of reaccretion of gas. The blastwave feedback model transfers SN energy directly to the surrounding gas particles in the form of thermal energy while simultaneously disabling cooling. As a result, gas particles may reach very high ($>10^5$ K) temperatures while temporarily retaining their high density. The subsequent reaccretion timescale will be affected by their ability to cool at high temperatures. Other feedback models that include less thermal heating of the gas, such as those using a hydrodynamically decoupled kinetic wind model (Springel & Hernquist 2003a), should be expected to cool and reaccrete more readily.

Another important numerical factor to consider with examining reaccretion rates in simulations is the presence of thermal instabilities in the halo. As SPH effectively refines in resolution based on density, the low-density regions of the halo are resolved to a lesser degree. As a result, instabilities and small-scale structure will be less accurately modeled. Such instabilities become most sensitive to numerics when a hot gaseous halo is present (Agertz et al. 2007). However, at the masses considered in this study, most simulations suggest that a

virial shock is not able to be supported (Birnboim & Dekel 2003; Kereš et al. 2005; though see Nelson et al. 2013).

The version of SPH used in this paper is known to suffer from spurious "surface tension" forces, which make it poor at modeling Kelvin–Helmholtz instabilities. However, Hopkins et al. (2014) showed that the changes due to different SPH modeling were insignificant compared to the feedback models chosen. Furthermore, the net amount of gas accretion (as opposed to its thermal state) appears to be fairly consistent across different hydrodynamic implementations (Nelson et al. 2013). Until a complete suite of high-resolution galaxies can be simulated with a modified version of the SPH formalism (J. Wadsley et al. 2016, in preparation) or a new hydrodynamics methodology (e.g., Hopkins 2015), these simulations represent our most complete understanding of the scaling outflow properties with mass.

5. CONCLUSIONS

Using high-resolution simulations, we have compared the outflow properties of 20 galaxy halos spanning the mass range of $10^{9.5}$–$10^{12}\,M_{\odot}$ using particle tracking to identify and follow outflowing gas. We show that the resulting galaxies match observed global galaxy properties, indicating that their baryonic content is realistic in terms of stellar mass, metallicity, and kinematics.

Since these trends are determined in a large part by the rates of gas inflow and outflow, these simulated galaxies present an opportunity to analyze the properties of outflows that plausibly produce realistic galaxies. We track gas particles to identify pristine gas accretion, recycled accretion, and gas leaving the disk and/or the halo. From this tracking we were able to determine the efficiency of outflows, the relative mass of outflowing and recycled gas, and the properties of the gas both prior to outflow and after accretion. Since the stellar feedback recipe used in these simulations depended only on the local properties of the ISM (not the host galaxy properties), trends in the outflow properties with halo mass must result from the dynamics of the simulation.

Our conclusions are summarized as follows:

1. With decreasing galaxy mass, galaxies are significantly more efficient at generating outflows. Specifically, mass loading factors show a power-law dependency on circular velocity, with an exponent of ≈ -2, which is consistent with energy-driven wind models. The similarity between the scaling for the analytic solution and that measured for the simulations argues for the mass loading factor being primarily a function of the global halo properties; the greater efficiency of small galaxies at driving outflows is simply a result of their shallower potential well. Furthermore, there was no redshift evolution in the scaling of the mass loading factors, which is consistent with η being primarily a function of halo depth.
2. In L^{*} galaxies, ejective feedback is able to reduce the baryonic disk mass by 20%, while in galaxies with halo masses $\lesssim 10^{10}\,M_{\odot}$ there can be as large as an 80% mass reduction. These fractions are very similar to the stellar-to-disk mass ratio across a range of galaxy masses, indicating that ejective feedback is comparable in significance to the globally averaged star formation efficiency in setting the stellar mass of galaxies. Preventative feedback also plays an important role in setting the stellar mass fraction across the entire mass range; galaxies with masses lower than $10^{11}\,M_{\odot}$ had reduced baryon masses compared to the cosmic baryon fraction, and across the entire mass range only about half of the gas accreted onto the halo was later accreted onto the disk.
3. Recycling is shown to be a common feature of galaxy evolution. Approximately 50% of gas that becomes dynamically unbound from the disk (ejected) is later reaccreted across all masses of galaxies. Such recycling occurs primarily on short timescales. The median timescales are $\sim$1 Gyr, with very little dependence on halo mass, and the timescales follow a logarithmic fall-off.
4. The source of outflowing material roughly follows the spatial distribution of star formation. As such, gas is preferentially removed from the centers of galaxies. Gas is subsequently reaccreted with higher angular momenta and farther out in the disk, indicating that it is "spun up" through interactions with the halo. This trend is consistent with previous work indicating that feedback-driven outflows can have a significant impact on the angular momentum distribution of disk baryons.

These results give a quantitative picture for how preventive feedback, ejective feedback, and star formation efficiency plausibly combine to yield the baryon fractions in galaxies seen today. In L^{*} halos, the $\sim$25% efficiency of baryonic conversion into stars is primarily driven by the inability of baryons in the halo to accrete onto the disk, presumably owing to the rapid growth of a hot hydrostatic halo (e.g., Dekel et al. 2009; Gabor & Bournaud 2014). In modest-sized halos down to $\sim 3 \times 10^{10}\,M_{\odot}$, ejective feedback becomes the dominant modulator of star formation, as large-scale cosmological models often assume. At smaller (dwarf) masses, all three effects are comparably important: there is significant prevention of accretion onto the halo, there is an increasing ejection rate, and of the material remaining in the disk, less is formed into stars.

A large number of the outflow properties we examined are mostly independent of halo mass. Lower-mass galaxies were more efficient at producing outflows, in terms of both their higher mass loading factors and the higher fractions of disk gas that was ejected. Indeed, the scaling of the mass loading factor with circular velocity calculated from our simulations is consistent with previous observations (Rupke et al. 2005; Arribas et al. 2014; Chisholm et al. 2015). In contrast, the gas that was ejected from the disk tends to have similar $v/v_{\rm circ}$, recycling times, and reaccreted fractions across all halo masses. These similarities indicate that reducing the galaxy mass lowers the threshold for driving outflows, but that the outflows themselves are quite similar across galaxy mass when scaled by the relevant galaxy property. This is somewhat remarkable given the complex driving mechanisms and interplay of outflowing gas with ambient ISM and halo material.

Together, our results strongly argue for galactic outflows being fundamental to setting the mass of baryons and their distribution within galaxies. Metallicities offer yet another strong constraint on the history of the baryon cycle. Future work will analyze the source of metals, their eventual location, and the relative rates of pristine versus enriched accretion. Such metal distribution mechanisms can be directly constrained by observations of metal absorption lines in quasar spectra passing

near galaxies, such as that obtained from the COS-Halos program (Tumlinson et al. 2011; Ford et al. 2016).

The authors are grateful for the referee's helpful suggestions. They would like to thank Rachel Somerville for her insightful feedback. These simulations were run at NASA AMES and Texas Supercomputing Center. C.C. acknowledges support from NSF grants AST-0908499 and AST-1009452. F.G. acknowledges support from grants *HST* GO-1125, NSF AST-0908499, and AST-1410012, and NASA ATP13-0020. T.Q. acknowledges support from NSF grant AST-0908499 and NSF AST-1311956. R.D. acknowledges support from the South African Research Chairs Initiative and the South African National Research Foundation. This research was also supported in part by the NSF under grant No. NSF PHY11-25915 and AST-0847667 and by NASA grant NNX12AH86G.

REFERENCES

Abel, T., Anninos, P., Zhang, Y., & Norman, M. L. M. L. 1997, NewA, 2, 181
Agertz, O., & Kravtsov, A. V. 2014, ApJ, 804, 18
Agertz, O., Moore, B., Stadel, J., et al. 2007, MNRAS, 380, 963
Aguirre, A., Hernquist, L., Schaye, J., et al. 2001, ApJ, 561, 521
Andrews, B. H., & Martini, P. 2013, ApJ, 765, 140
Anglés-Alcázar, D., Davé, R., Özel, F., & Oppenheimer, B. D. 2014, ApJ, 782, 84
Arribas, S., Colina, L., Bellocchi, E., Maiolino, R., & Villar-Martín, M. 2014, A&A, 568, A14
Aumer, M., White, S. D. M., Naab, T., & Scannapieco, C. 2013, MNRAS, 434, 3142
Balogh, M. L. M. L., Pearce, F. R., Bower, R. G., & Kay, S. T. 2001, MNRAS, 326, 1228
Behroozi, P. S., Wechsler, R. H., & Conroy, C. 2013, ApJ, 770, 57
Bigiel, F., Leroy, A. K., Walter, F., et al. 2008, AJ, 136, 2846
Binney, J., Gerhard, O., & Silk, J. 2001, MNRAS, 321, 471
Birnboim, Y., & Dekel, A. 2003, MNRAS, 345, 349
Black, J. H. J. H. 1981, MNRAS, 197, 553
Bower, R. G., Benson, A. J., & Crain, R. A. 2012, MNRAS, 422, 2816
Brook, C. B., Cintio, A. D., Knebe, A., et al. 2014, ApJL, 784, L14
Brook, C. B., Governato, F., Roškar, R., et al. 2011, MNRAS, 415, 1051
Brook, C. B., Stinson, G., Gibson, B. K., et al. 2012a, MNRAS, 419, 771
Brook, C. B., Stinson, G., Gibson, B. K., Wadsley, J., & Quinn, T. 2012b, MNRAS, 424, 1275
Brooks, A. M., Governato, F., Booth, C. M., et al. 2007, ApJL, 655, L17
Cen, R. 1992, ApJS, 78, 341
Cen, R., & Chisari, N. E. 2011, ApJ, 731, 11
Ceverino, D., Klypin, A., Klimek, E., et al. 2014, MNRAS, 442, 1545
Chevalier, R. A. 1974, ApJ, 188, 501
Chevalier, R. A., & Clegg, A. W. 1985, Natur, 317, 44
Chisholm, J., Tremonti, C. A., Leitherer, C., et al. 2015, ApJ, 811, 149
Christensen, C., Quinn, T., Governato, F., et al. 2012, MNRAS, 425, 3058
Christensen, C. R., Brooks, A. M., Fisher, D. B., et al. 2014a, MNRAS, 440, L51
Christensen, C. R., Governato, F., Quinn, T., et al. 2014b, MNRAS, 440, 2843
Cowie, L. L., Songaila, A., Kim, T.-S., & Hu, E. M. 1995, AJ, 109, 1522
Dalcanton, J. J., Spergel, D. N., & Summers, F. J. 1997, ApJ, 482, 659
Davé, R. 2009, in ASP Conf. Ser. 419, Galaxy Evolution: Emerging Insights and Future Challenges, ed. S. Jogee et al. (San Francisco, CA: ASP), 347
Davé, R., Finlator, K., & Oppenheimer, B. D. 2012, MNRAS, 421, 98
Dave, R., Katz, N., Oppenheimer, B. D., Kollmeier, J. A., & Weinberg, D. H. 2013, MNRAS, 434, 2645
Davé, R., Oppenheimer, B. D., & Finlator, K. 2011, MNRAS, 415, 11
Davé, R., Spergel, D. N., Steinhardt, P. J., & Wandelt, B. D. 2001, ApJ, 547, 574
Dekel, A., Birnboim, Y., Engel, G., et al. 2009, Natur, 457, 451
Dekel, A., & Silk, J. 1986, ApJ, 303, 39
Draine, B. T. B. T., & Bertoldi, F. 1996, ApJ, 468, 269
Erb, D. K. 2008, ApJ, 674, 151
Erb, D. K., Shapley, A. E., Pettini, M., et al. 2006, ApJ, 644, 813
Fall, S. M., & Efstathiou, G. 1980, MNRAS, 193, 189
Ferland, G. J., Korista, K. T., Verner, D. A., et al. 1998, PASP, 110, 761
Finlator, K., & Davé, R. 2008, MNRAS, 385, 2181
Ford, A. B., Davé, R., Oppenheimer, B. D., et al. 2014, MNRAS, 444, 1260
Ford, A. B., Werk, J. K., Dave, R., et al. 2016, MNRAS, 459, 1745
Gabor, J. M., & Bournaud, F. 2014, MNRAS, 437, L56
Geha, M., Blanton, M. R., Masjedi, M., & West, A. A. 2006, ApJ, 653, 240
Genel, S., Vogelsberger, M., Springel, V., et al. 2014, MNRAS, 445, 175
Genzel, R., Newman, S., Jones, T., et al. 2011, ApJ, 733, 101
Genzel, R., Tacconi, L. J., Kurk, J., et al. 2013, ApJ, 773, 68
Gill, S. P. D., Knebe, A., & Gibson, B. K. 2004, MNRAS, 351, 399
Glover, S. C. O., & Mac Low, M.-M. 2007, ApJS, 169, 239
Gnedin, N. Y. 2000, ApJ, 535, 530
Gnedin, N. Y., Tassis, K., & Kravtsov, A. V. 2009, ApJ, 697, 55
Governato, F., Brook, C. B., Brooks, A. M., et al. 2009, MNRAS, 398, 312
Governato, F., Brook, C. B., Mayer, L., et al. 2010, Natur, 463, 203
Governato, F., Zolotov, A., Pontzen, A., et al. 2012, MNRAS, 422, 1231
Haardt, F., & Madau, P. 1996, ApJ, 461, 20
Henriques, B. M. B., White, S. D. M., Thomas, P. A., et al. 2013, MNRAS, 431, 3373
Hoeft, M., Yepes, G., Gottlöber, S., & Springel, V. 2006, MNRAS, 371, 401
Hopkins, P. F. 2015, MNRAS, 450, 53
Hopkins, P. F., Keres, D., Onorbe, J., et al. 2014, MNRAS, 445, 581
Jonsson, P. 2006, MNRAS, 372, 2
Kannan, R., Stinson, G. S., Maccío, A. V., et al. 2014, MNRAS, 437, 3529
Katz, N., & White, S. D. M. 1993, ApJ, 412, 455
Keller, Ã., Wadsely, Ã., & Couchman, Ã. 2015, MNRAS, 453, 3499
Keller, B. W., Wadsley, J., Benincasa, S. M., & Couchman, H. M. P. 2014, MNRAS, 442, 3013
Kereš, D., Katz, N., Weinberg, D. H., et al. 2005, MNRAS, 363, 2
Kewley, L. J., & Ellison, S. L. 2008, ApJ, 681, 1183
Knollmann, S. R. S. R., & Knebe, A. 2009, ApJS, 182, 608
Lee, H., Skillman, E. D., Cannon, J. M., et al. 2006, ApJ, 647, 970
Macciò, A. V., Stinson, G. S., Brook, C. B., et al. 2012, ApJL, 744, L9
Marasco, A., Fraternali, F., & Binney, J. J. 2012, MNRAS, 419, 1107
Martin, C. L. 2005, ApJ, 621, 227
McGaugh, S. S. 2005, ApJ, 632, 859
McKee, C. F., & Ostriker, J. P. 1977, ApJ, 218, 148
Mitra, S., Davé, R., & Finlator, K. 2015, MNRAS, 452, 1184
Mo, H. J., & Mao, S. 2002, MNRAS, 333, 768
Mo, H. J. J., Mao, S., & White, S. D. M. 1998, MNRAS, 295, 319
Moster, B. P., Naab, T., & White, S. D. M. 2013, MNRAS, 428, 3121
Munshi, F., Governato, F., Brooks, A. M., et al. 2013, ApJ, 766, 56
Muratov, A. L., Keres, D., Faucher-Giguere, C.-A., et al. 2015, MNRAS, 454, 2691
Murray, N., Quataert, E., & Thompson, T. A. 2005, ApJ, 618, 569
Navarro, J. F., & Steinmetz, M. 1997, ApJ, 478, 13
Navarro, J. F., & Steinmetz, M. 2000, ApJ, 528, 607
Nelson, D., Vogelsberger, M., Genel, S., et al. 2013, MNRAS, 429, 3353
Okamoto, T., Eke, V. R., Frenk, C. S., & Jenkins, A. 2005, MNRAS, 363, 1299
Okamoto, T., Gao, L., & Theuns, T. 2008, MNRAS, 390, 920
Oppenheimer, B. D., & Davé, R. 2008, MNRAS, 387, 577
Oppenheimer, B. D., Davé, R., & Dave, R. 2006, MNRAS, 373, 1265
Oppenheimer, B. D., Davé, R., Katz, N., Kollmeier, J. A., & Weinberg, D. H. 2012, MNRAS, 420, 829
Oppenheimer, B. D., Davé, R., Kereš, D., et al. 2010, MNRAS, 406, 2325
Peeples, M. S., & Shankar, F. 2011, MNRAS, 417, 2962
Pettini, M., Madau, P., Bolte, M., et al. 2003, ApJ, 594, 695
Pizagno, J., Prada, F., Weinberg, D. H., et al. 2007, AJ, 134, 945
Raiteri, C. M., Villata, M., & Navarro, J. F. 1996, A&A, 315, 105
Robertson, B. E., Yoshida, N., Springel, V., et al. 2004, ApJ, 606, 32
Rubin, K. H. R., Prochaska, J. X., Koo, D. C., et al. 2014, ApJ, 794, 156
Rupke, D. S., Veilleux, S., & Sanders, D. B. 2005, ApJS, 160, 115
Scannapieco, C., Tissera, P. B., White, S. D. M., & Springel, V. 2008, MNRAS, 389, 1137
Scannapieco, C., Wadepuhl, M., Parry, O. H., et al. 2012, MNRAS, 423, 1726
Shankar, F., Lapi, A., Salucci, P., De Zotti, G., & Danese, L. 2006, ApJ, 643, 14
Shapley, A. E., Steidel, C. C., Pettini, M., & Adelberger, K. L. 2003, ApJ, 588, 65
Shen, S., Madau, P., Conroy, C., Governato, F., & Mayer, L. 2014, ApJ, 792, 99
Shen, S., Wadsley, J., & Stinson, G. S. 2010, MNRAS, 407, 1581
Somerville, R. S., Popping, G., & Trager, S. 2015, MNRAS, 453, 4337
Spergel, D. N., Bean, R., Doré, O., et al. 2007, ApJS, 170, 377
Springel, V., & Hernquist, L. 2003a, MNRAS, 339, 289
Springel, V., & Hernquist, L. 2003b, MNRAS, 339, 312
Stadel, J. 2001, PhD thesis, Univ. Washington

Steidel, C. C., Erb, D. K. D. K., Shapley, A. E., et al. 2010, ApJ, 717, 289
Steinmetz, M., & Navarro, J. F. 1999, ApJ, 513, 555
Stinson, G. S., Brook, C., Maccio, A. V., et al. 2012, MNRAS, 428, 129
Stinson, G. S., Seth, A. C., Katz, N., et al. 2006, MNRAS, 373, 1074
Tremonti, C. A., Heckman, T. M., Kauffmann, G., et al. 2004, ApJ, 613, 898
Tumlinson, J., Thom, C., Werk, J. K., et al. 2011, Sci, 334, 948
Übler, H., Naab, T., Oser, L., et al. 2014, MNRAS, 443, 2092
van de Voort, F., Schaye, J., Booth, C. M., Haas, M. R., & Dalla Vecchia, C. 2011, MNRAS, 414, 2458
van den Bosch, F. C., Burkert, A., & Swaters, R. A. 2001, MNRAS, 326, 1205
Verner, D. A. A., & Ferland, G. J. J. 1996, ApJS, 103, 467
Vogelsberger, M., Genel, S., Springel, V., et al. 2014, MNRAS, 444, 1518
Wadsley, J., Stadel, J., & Quinn, T. R. 2004, NewA, 9, 137
Wang, L., Dutton, A. A., Stinson, G. S., et al. 2015, MNRAS, 454, 83
Weidemann, V. 1987, A&A, 188, 74
Weiner, B. J., Coil, A. L. A. L., Prochaska, J. X., et al. 2009, ApJ, 692, 187
White, S. D. M., & Rees, M. J. 1978, MNRAS, 183, 341
Wolfire, M. G., Tielens, A. G. G. M., Hollenbach, D. J., & Kaufman, M. J. 2008, ApJ, 680, 384
Woods, R. M., Wadsley, J., Couchman, H. M. P., Stinson, G., & Shen, S. 2014, MNRAS, 442, 732
Zolotov, A., Brooks, A. M., Willman, B., et al. 2012, ApJ, 761, 71